Monthly Notices
of the
ROYAL ASTRONOMICAL SOCIETY

MNRAS **461,** 93–110 (2016)
Advance Access publication 2016 June 7

doi:10.1093/mnras/stw1323

# Sub-mm emission line deep fields: CO and [C II] luminosity functions out to $z = 6$

Gergö Popping,[1]★ Eelco van Kampen,[1] Roberto Decarli,[2] Marco Spaans,[3] Rachel S. Somerville[4] and Scott C. Trager[3]

[1]*European Southern Observatory, Karl-Schwarzschild-Strasse 2, D-85748, Garching, Germany*
[2]*Max-Planck Institut für Astronomie, Königstuhl 17, D- 69117, Heidelberg, Germany*
[3]*Kapteyn Astronomical Institute, University of Groningen, Postbus 800, NL-9700 AV Groningen, the Netherlands*
[4]*Department of Physics and Astronomy, Rutgers University, 136 Frelinghuysen Road, Piscataway, NJ 08854, USA*

Accepted 2016 June 1. Received 2016 May 27; in original form 2016 February 8

## ABSTRACT

Now that Atacama Large (Sub)Millimeter Array is reaching its full capabilities, observations of sub-mm emission line deep fields become feasible. We couple a semi-analytic model of galaxy formation with a radiative transfer code to make predictions for the luminosity function of CO J =1–0 out to CO J = 6–5 and [C II] at redshifts $z$= 0–6. We find that (1) our model correctly reproduces the CO and [C II] emission of low- and high-redshift galaxies and reproduces the available constraints on the CO luminosity function at $z \leq 2.75$; (2) we find that the CO and [C II] luminosity functions of galaxies increase from $z = 6$ to $z = 4$, remain relatively constant till $z = 1$ and rapidly decrease towards $z = 0$. The galaxies that are brightest in CO and [C II] are found at $z \sim 2$; (3) the CO J = 3–2 emission line is most favourable to study the CO luminosity and global $H_2$ mass content of galaxies, because of its brightness and observability with currently available sub-mm and radio instruments; (4) the luminosity functions of high-J CO lines show stronger evolution than the luminosity functions of low-J CO lines; (5) our model barely reproduces the available constraints on the CO and [C II] luminosity function of galaxies at $z \geq 1.5$ and the CO luminosity of individual galaxies at intermediate redshifts. We argue that this is driven by a lack of cold gas in galaxies at intermediate redshifts as predicted by cosmological simulations of galaxy formation.

**Key words:** ISM: atoms – ISM: lines and bands – ISM: molecules – galaxies: evolution – galaxies: formation – galaxies: ISM.

## 1 INTRODUCTION

Our understanding of galaxy formation and evolution has grown a lot based on the contribution by deep blind fields. These deep fields mostly focused on the X-ray, optical, near-infrared, sub-mm continuum, and radio wavelengths. They have contributed tremendously to our understanding of the star formation (SF) history of our Universe and the stellar build-up of galaxies and have allowed us to derive a number of galaxy properties such as stellar masses, star formation rates (SFR), morphologies, and sizes. In particular, it has been shown that the SF history of our Universe peaked at redshifts $z \sim 2$–3, after which it dropped to its present-day value (e.g. Madau et al. 1996; Hopkins 2004; Hopkins & Beacom 2006, for a recent review see Madau & Dickinson 2014).

The *Herschel Space Observatory* (Pilbratt et al. 2010) has made significant contributions to our understanding of galaxy formation and evolution by observing deep fields of the sub-mm continuum of galaxies (e.g. Eales et al. 2010; Oliver et al. 2012). The Atacama Large (Sub)Millimeter Array (ALMA) allows us to observe deep fields at sub-mm wavelengths with higher sensitivity and over a larger continuous range of wavelengths. Additionally, the angular resolution of interferometers such as ALMA and the Plateau de Bure Interferometer/Northern Extended Millimeter Array (NOEMA) allows us to pinpoint individual galaxies with much better accuracy compared to single dish observatories (Decarli et al. 2014b; Walter et al. 2014). Similar exercises can be carried out with the Jansky Very Large Array (JVLA) and in the near future the next generation VLA (ngVLA; Carilli et al. 2015; Casey et al. 2015). Such efforts can reveal the properties of atomic and molecular gas in galaxies, a baryonic component not yet addressed in deep surveys other than local H I efforts (Barnes et al. 2001; Giovanelli et al. 2005).[1]

Deep surveys are rather expensive, but have advantages over surveys targeting galaxies based on their stellar masses and/or SFRs.

★ E-mail: gpopping@eso.org

[1] Damped Lyman $\alpha$ surveys have contributed greatly to our understanding of the global budget of H I in our Universe out to redshifts of ∼5–6 (e.g. Prochaska & Wolfe 2009; Crighton et al. 2015).

First of all, blind surveys allow us to detect new classes of objects previously missed in targeted surveys due to for example stellar masses and SFRs not fulfilling the selection criteria. More relevant to this work, blind surveys are ideal to assess the number densities of different classes of galaxies. With this in mind, blind surveys with radio and sub-mm instruments are perfectly suited to observe the luminosity function of the sub-mm continuum of galaxies down to faint luminosities and high redshifts. Furthermore, due to the high spectral resolution, we are entering an exciting new era where we can observe the luminosity function of sub-mm emission lines such as different CO rotational transitions and [C II]. In this paper, we make predictions for future efforts focusing on the luminosity function of different CO transitions and [C II] based on a semi-analytic model of galaxy formation coupled to a radiative transfer code.

Because of its high abundance ($\sim 10^{-4}$ in Milky Way-type galaxies) CO is a bright tracer of the molecular interstellar medium (ISM) in galaxies. A survey focusing on CO can therefore effectively trace and provide constraints on the reservoir of gas potentially available for SF (Walter et al. 2014). Due to its brightness, [C II] is one of the first emission lines that can be picked up with sub-mm instruments, which makes it a valuable line to find new objects through blind surveys, or assign spectroscopic redshifts (see for a review Carilli & Walter 2013). In local galaxies, [C II] emission correlates with SF (de Looze et al. 2011; Herrera-Camus et al. 2015), which makes it an extra worthwhile emission line to go after.

Constraints on the gas content of galaxies are crucial for theoretical models of galaxy formation. This information is necessary to break the degeneracies between different physical mechanisms included in theoretical models such as metal enrichment and feedback processes. At the same time, models have the potential to provide a theoretical context for sub-mm emission line deep fields, as this is still an unexplored field.

Recently, theoretical models of galaxy formation started to include recipes to model the sub-mm line emission from galaxies (e.g. Narayanan et al. 2008; Obreschkow et al. 2009; Pérez-Beaupuits, Wada & Spaans 2011; Feldmann, Gnedin & Kravtsov 2012; Lagos et al. 2012; Popping et al. 2014b; Olsen et al. 2015a,b). Semi-analytic models in particular are a powerful tool to make predictions for CO and [C II] luminosity functions. Within the semi-analytic framework, simplified but physically motivated recipes are used to track physical processes such as the cooling of hot gas into galaxies, SF, the energy input from supernovae and active galactic nuclei into the ISM, the sizes of galaxy discs, and the enrichment of the ISM by supernovae ejecta and stellar winds (see Somerville & Davé 2015, for a recent review). The low computational cost of semi-analytic models makes them a powerful tool to model large volumes on the sky and provide robust predictions for deep field studies.

In this work, we use an updated version of the model presented in Popping et al. (2014b, hereafter P14), where we coupled a radiative transfer model to the Popping, Somerville & Trager (2014a, hereafter PST14) semi-analytical model. The PST14 model has proven to be successful in reproducing observations of the H I and $H_2$ content of galaxies in the local and high-redshift Universe, such as stellar mass–gas mass relations, the local H I and $H_2$ mass functions, and the sizes of the gas discs of galaxies. The P14 model successfully reproduces the CO, [C II], and atomic carbon luminosity of local and high-redshift galaxies. Updates to the approach presented in P14 concern the coupling between the semi-analytic model and the radiative transfer code, as well as the sub-grid treatment of molecular cloud structures. We will present these updates in Section 2.

This paper is structured as follows. In Section 2, we present the theoretical model to make predictions for the CO and [C II] emission of galaxies. We compare model predictions for the scaling relation between sub-mm lines emission and far-infrared (FIR) luminosity and SFR with observations of local and high-redshift galaxies in Section 3. We present our predictions for the CO and [C II] luminosity functions out to $z = 6$ in Section 4. We discuss our findings in Section 5 and summarize our work in Section 6. Throughout this paper, we adopt a flat $\Lambda$ cold dark matter ($\Lambda$CDM) cosmology with $\Omega_0 = 0.28$, $\Omega_\Lambda = 0.72$, $h = H_0/(100\,\mathrm{km\,s^{-1}\,Mpc^{-1}}) = 0.7$, $\sigma_8 = 0.812$, and a cosmic baryon fraction of $f_b = 0.1658$ (Komatsu et al. 2009).

## 2 MODEL DESCRIPTION

### 2.1 Galaxy formation model

The galaxy formation model used to create a mock sample of galaxies within a $\Lambda$CDM cosmology was originally presented in Somerville & Primack (1999) and Somerville, Primack & Faber (2001). Significant updates to this model are described in Somerville et al. (2008), Somerville et al. (2012), Porter et al. (2014), PST14, and Somerville, Popping & Trager (2015, hereafter SPT15). The model tracks the hierarchical clustering of dark matter haloes, shock heating and radiative cooling of gas, SN feedback, SF, active galactic nucleus feedback (by quasars and radio jets), metal enrichment of the interstellar and intracluster medium, mergers of galaxies, starbursts, the evolution of stellar populations, and dust obscuration. The PST14 and SPT15 models include new recipes that track the abundance of ionized, atomic, and molecular hydrogen, and a molecule-based SF recipe. Here, we briefly summarize the recipes employed to track the molecular hydrogen abundance and the molecule-based SF recipe, as these set the molecular hydrogen abundance and UV radiation field in Section 2.2. We point the reader to Somerville et al. (2008), Somerville et al. (2012), PST14, and SPT15 for a more detailed description of the model.

To compute the $H_2$ fraction of the cold gas, we use an approach based on the work by Gnedin & Kravtsov (2011). The authors performed high-resolution 'zoom-in' cosmological simulations with the Adaptive Refinement Tree (ART) code (Kravtsov 1999), including gravity, hydrodynamics, non-equilibrium chemistry, and simplified 3D on-the-fly radiative transfer (Gnedin & Kravtsov 2011). The authors find a simple fitting formula for the $H_2$ fraction of cold gas based on the dust-to-gas ratio relative to solar, $D_{\rm MW}$, the ionizing background radiation field, $U_{\rm MW}$, and the surface density of the cold gas, $\Sigma_{\rm H\,I+H2}$. The fraction of molecular hydrogen is given by

$$f_{\rm H_2} = \left[1 + \frac{\tilde{\Sigma}}{\Sigma_{\rm H\,I+H_2}}\right]^{-2}, \quad (1)$$

where

$$\tilde{\Sigma} = 20\,{\rm M_\odot pc^{-2}}\,\frac{\Lambda^{4/7}}{D_{\rm MW}}\,\frac{1}{\sqrt{1+U_{\rm MW}D_{\rm MW}^2}},$$

$$\Lambda = \ln(1 + g\,D_{\rm MW}^{3/7}(U_{\rm MW}/15)^{4/7}),$$

$$g = \frac{1+\alpha s + s^2}{1+s},$$

$$s = \frac{0.04}{D_* + D_{\rm MW}},$$

$$\alpha = 5\frac{U_{\rm MW}/2}{1+(U_{\rm MW}/2)^2},$$

$$D_* = 1.5\times10^{-3}\ \ln(1+(3U_{\rm MW})^{1.7}).$$

We assume that the dust-to-gas ratio is proportional to the metallicity of the gas in solar units $D_{\rm MW} = Z_{\rm gas}/Z_\odot$. We assume that the local UV background scales with the SFR relative to the Milky Way value, $U_{\rm MW} = {\rm SFR}/{\rm SFR}_{\rm MW}$, where we choose ${\rm SFR}_{\rm MW} = 1.0\,{\rm M}_\odot\ {\rm yr}^{-1}$ (Murray & Rahman 2010; Robitaille & Whitney 2010). Following Gnedin & Kravtsov (2011), we take $n_* = 25{\rm cm}^{-3}$.

We considered other recipes for the partitioning of H I and $H_2$ in PST14 and SPT15. We found that metallicity-based recipes that do not include a dependence on the UV background predict less efficient formation of $H_2$, less SF, and less metal enrichment at early times in low-mass haloes ($M_{\rm h} < 10^{10.5}\,{\rm M}_\odot$). PST14 also considered a pressure-based recipe (Blitz & Rosolowsky 2006), but found that the pressure-based version of the model is less successful in reproducing the H I density of our Universe at $z > 0$.

The SF in the semi-analytic model (SAM) is modelled based on an empirical relationship between the surface density of molecular hydrogen and the surface density of SF (Bigiel et al. 2008; Genzel et al. 2010; Bigiel & Blitz 2012). Observations of high-density environments (especially in starbursts and high-redshift objects) have indicated that above some critical surface density, the relation between molecular hydrogen surface density and SFR surface density steepens (Sharon et al. 2013; Hodge et al. 2015). To account for this steepening, we use the following expression to model SF:

$$\Sigma_{\rm SFR} = A_{\rm SF}\,\Sigma_{\rm H_2}/(10\,{\rm M}_\odot\,{\rm pc}^{-2})\left(1+\frac{\Sigma_{\rm H_2}}{\Sigma_{\rm H_2,crit}}\right)^{N_{\rm SF}}, \quad (2)$$

where $\Sigma_{\rm H_2}$ is the surface density of molecular hydrogen and with $A_{\rm SF} = 5.98\times10^{-3}\ {\rm M}_\odot\ {\rm yr}^{-1}\ {\rm kpc}^{-2}$, $\Sigma_{\rm H_2,crit} = 70\,{\rm M}_\odot\ {\rm pc}^{-2}$, and $N_{\rm SF} = 1$.

The sizes of the galaxy discs are important as they set the surface densities for our $H_2$ partitioning recipe and SF relation, but will also control the volume density of the gas when calculating the line emission from atoms and molecules. When gas cools on to a galaxy, we assume it initially collapses to form a rotationally supported disc. The scale radius of the disc is computed based on the initial angular momentum of the gas and the halo profile, assuming that angular momentum is conserved and that the self-gravity of the collapsing baryons causes contraction of the matter in the inner part of the halo (Blumenthal et al. 1986; Flores et al. 1993; Mo, Mao & White 1998). This approach has shown to successfully reproduce the evolution of the size–stellar mass relation of disc-dominated galaxies from $z \sim 2$ to $z = 0$. PST14 successfully reproduced the sizes of H I discs in the local Universe and the observed sizes of CO discs in local and high-redshift galaxies using this approach.

We use the approach presented in Arrigoni et al. (2010) to track the carbon abundance of the ISM. Arrigoni et al. (2010) extended the Somerville et al. semi-analytic model to include the detailed metal enrichment by Type Ia and Type II supernovae and long-lived stars. With this extension our model tracks the abundances of 19 individual elements.

FIR luminosities are calculated using the approach presented in Somerville et al. (2012). Emission is absorbed by two components. One is diffuse dust in the disc and the other is associated with the birth clouds surrounding young star-forming regions. It is then assumed that all the energy emitted by stars that is absorbed by dust is re-radiated in the infrared.

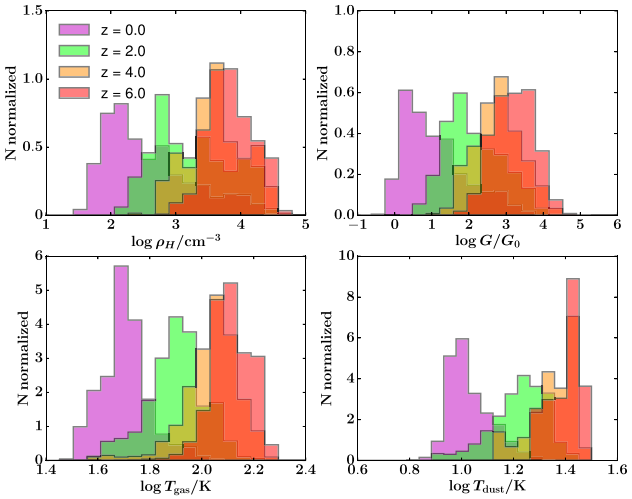


**Figure 1.** The distribution of the density-weighted average gas density (top left), UV radiation field (top right), gas temperature (bottom left), and dust temperature (bottom right) for central star-forming galaxies at redshifts $z = 0, 2, 4$, and 6.

### 2.2 Creating a 3D realization of the ISM

SAMs are a very powerful tool to model the global properties of galaxies (such as cold gas mass, SFR, stellar mass, and size). However, they lack detailed information on the spatial distribution of baryons within a galaxy. In this subsection, we describe the recipes used to create a 3D realization at parsec-level resolution of the mock sample of galaxies created by the SAM.

#### *2.2.1 Gas density*

Under the assumption that cold gas (H I + $H_2$) follows an exponential distribution in the radial and vertical direction, the hydrogen density at any point in the galaxy at radius $r$ and height $z$ is described as

$$n_{\rm H}(r,z) = n_0(r)\,\exp\left(-\frac{r}{R_{\rm g}}\right)\exp\left(-\frac{|z|}{z_{\rm g}(r)}\right), \quad (3)$$

where $n_0(r)$ is the central hydrogen density at any radius $r$, $R_{\rm g}$ the gas scalelength of the galaxy and $z_{\rm g}(r)$ the gas scaleheight.

The central hydrogen density $n_0(r)$ is given by

$$n_0(r) = \frac{M_{\rm H}}{4\pi m_{\rm H}\,R_{\rm g}^2 z_{\rm g}(r)}, \quad (4)$$

where $M_{\rm H}$ is the total hydrogen mass (atomic plus molecular) of the galaxy and $m_{\rm H}$ the mass of a single hydrogen atom.

We assume that the gaseous disc is in vertical equilibrium, where the gravitational force is balanced by the pressure of the gas. Following Popping et al. (2012) and P14, we can then express $z_{\rm g}(r)$ as

$$z_{\rm g}(r) = \frac{\sigma_{\rm gas}^2}{\pi G\left[\Sigma_{\rm gas}(r)+0.1\sqrt{\Sigma_*(r)\Sigma_*^0}\right]}, \quad (5)$$

where $\Sigma_*(r)$ is the stellar surface density, and $\Sigma_*^0$ the central stellar surface density defined as $\frac{M_*}{2\pi r_*^2}$, with $M_*$ and $r_*$ the stellar mass and scalelength of the stellar disc, respectively. When constructing the gas density profile of the galaxy, we adopt a resolution of 200 pc and integrate the disc out to eight times its scale radius. We plot a distribution of the density-weighted average gas density of the modelled galaxies in Fig. 1. A more detailed description of the plot will be given in Section 3.

#### 2.2.2 $H_2$ abundance

The local $H_2$ abundance of cold gas is dependent on the local cold gas (column) density, whereas SAMs only provide the global $H_2$ abundance. The local $H_2$ abundance is one of the key ingredients when calculating the level populations of our atoms and molecules of interest. We therefore calculate the local $H_2$ abundance in every grid cell again following the results by Gnedin & Kravtsov (2011). This time the local $H_2$ abundance is a function of gas volume density rather than surface density, together with the previously defined dust-to-gas ratio relative to solar $D_{\rm MW}$, and the ionizing background radiation field $U_{\rm MW}$ (see Section 2.1). The local fraction of molecular hydrogen is now given by

$$f_{\rm H_2} = \frac{1}{1+\exp\left(-4x\,-\,3x^3\right)}, \tag{6}$$

where

$$x = \Lambda^{3/7}\ln\left(D_{\rm MW}\frac{n_{\rm H}}{\Lambda n_*}\right),$$

$$\Lambda = \ln\left(1+g\,D_{\rm MW}^{3/7}(U_{\rm MW}/15)^{4/7}\right),$$

$$g = \frac{1+\alpha s+s^2}{1+s},$$

$$s = \frac{0.04}{D_*+D_{\rm MW}},$$

$$\alpha = 5\frac{U_{\rm MW}/2}{1+(U_{\rm MW}/2)^2},$$

$$D_* = 1.5\times10^{-3}\ \ln(1+(3U_{\rm MW})^{1.7}).$$

Following Gnedin & Kravtsov (2011), we take $n_* = 25\,{\rm cm}^{-3}$. We normalize the sum of the local $H_2$ masses to the global $H_2$ mass to assure that the global $H_2$ mass is conserved.

#### 2.2.3 Radiation field

We derive the FUV (6–13.6 eV) field strength, $G_{\rm UV}$, by relating the SFR density to the FUV-radiation field as

$$\frac{G_{\rm UV}}{G_0} = \frac{\rho_{\rm SFR}}{\rho^0_{\rm SFR}}, \tag{7}$$

where $\rho_{\rm SFR}$ is the density of SF in ${\rm M}_\odot\,{\rm yr}^{-1}\,{\rm kpc}^{-3}$, $\rho^0_{\rm SFR}$ is the average SFR density in the MW, and $G_0 = 1.6\times10^{-3}\,{\rm erg\,cm}^{-2}\,{\rm s}^{-1}$ (the Habing Flux). We scale the density of SF as a function of the molecular hydrogen density in every grid cell with $\rho_{\rm SFR} = \rho^{1.5}_{\rm H2}$, normalizing it such that the total integrated SFR equals the SFR as predicted by our SAM. We take $\rho^0_{\rm SFR} = 0.0024\ {\rm M}_\odot\,{\rm yr}^{-1}\,{\rm kpc}^{-3}$ (Olsen et al. 2015a), which corresponds to the SFR density in the central 10 kpc of our MW. The distribution of the density-weighted average UV radiation field in the modelled galaxies is shown in Fig. 1.

#### 2.2.4 Abundances

The CO abundance of the cold gas is calculated as the amount of carbon locked up in CO. The fraction of the carbon mass locked up in CO has an explicit dependence on metallicity. Following Wolfire, Hollenbach & McKee (2010), we calculate this fraction as

$$f_{\rm CO} = f_{\rm H2}{\rm e}^{-4\left(0.52-0.045\,\ln\frac{G_{\rm UV}/(1.7G_0)}{n_{\rm H}}-0.097\ln\frac{Z_{\rm gas}}{Z_\odot}\right)/A_V}, \tag{8}$$

where $A_V = n_{\rm H}R_{\rm grid}(Z_{\rm gas}/Z_\odot)/1.87\times10^{21}$ mag, with $R_{\rm grid}$ the size of a grid cell in cm.

The remaining carbon is either ionized or atomic. We assume that the atomic and ionized carbon are equally distributed at $A_V = 1$ mag. At $A_V = 0$ mag, all the carbon is ionized, whereas at $A_V = 10$ mag, only 10 per cent of the carbon is ionized. These numbers reach good agreement with predictions from Meijerink & Spaans (2005) for the typical range of densities and radiation fields relevant to our work. We perform logarithmic interpolation between these points to calculate the abundance of atomic and ionized carbon at any $A_V$.

#### 2.2.5 Temperature

We calculate the temperature of the gas and dust using the DESPOTIC package (Krumholz 2014). Unless stated otherwise, the physical parameters match the defaults in DESPOTIC.

The temperature of the cold gas and dust is set by a balance of heating and cooling processes. Heating terms that are included are cosmic ray heating, photoelectric heating, gravitational heating, and the exchange of energy between dust and gas. The primary cooling mechanism for the gas is line radiation. We take the cooling through CO, atomic carbon [C], and ionized carbon $C^+$ into account. We refer the reader to Krumholz (2014) for a detailed explanation of the different heating and cooling terms. We set the temperature of the cosmic microwave background (CMB) at the redshift of the galaxy as a lower limit on the gas and dust temperature. We note that the adopted approach for calculating temperature is a significant improvement with respect to P14, where a simplified model was assumed only including the cooling through oxygen and ionized carbon. The addition of CO cooling in the densest environments allows for lower temperatures, which additionally suppresses the amount of CO emission. We plot a distribution of the density-weighted average gas and dust temperatures of the galaxies in Fig. 1.

#### 2.2.6 Velocity field and turbulence

To trace the absorption of photons along the line-of-sight information about the velocity field of the galaxy is necessary. We derive the velocity field following the approach presented in P14, where the radial velocity profile of a galaxy is constructed based on a component from the bulge, disc, and halo, respectively. We assume a vertical velocity dispersion $\sigma_{\rm gas}$ of $10\,{\rm km\,s}^{-1}$ (Leroy et al. 2008). The local non-thermal turbulent velocity dispersion is derived as the standard deviation of the velocities in the nearest neighbouring cells in all directions.

### 2.3 Radiative-transfer and line tracing

We use an updated version of the advanced fully 3D radiative-transfer code $\beta$3D (Poelman & Spaans 2005, 2006), optimized for heavy memory usage by Pérez-Beaupuits et al. (2011). To calculate the level populations of the molecule or atom of interest, $\beta$3D takes the escape probability of photons out of a molecular cloud along six directions into account. The optimized version was initially developed to calculate the 3D transfer of line radiation in 256 × 256 × 128 element data cubes at a spatial resolution of 0.25 pc. P14 optimized this code to calculate the line properties of galaxy-sized objects with much lower spatial resolution.

Calculating the emitted radiation from an atomic or molecular species requires solving for the number density of atoms or

molecules in the level of interest. It also requires calculating the probability that a photon at some position in the cloud can escape the system. The basic assumption in the radiative transfer calculation is that the levels of the atomic or molecular species are in statistical equilibrium. This implies that the rate of transitions out of each level is balanced by the rate of transitions into that level. For a multilevel molecule, this can be expressed using the equations of statistical equilibrium for each bound level $i$, with population density $n_i$, and energy $E_i$, as

$$n_i \sum_j R_{ij} = \sum_j n_j R_{ji}, \tag{9}$$

where the sums are over all other bound levels $j$. $R_{ij}$ gives the rate at which transitions from level $i$ to $j$ occur. These equations are supplemented by the constraint that the sum of all populations $n_i$ equals the density of the atomic or molecular species $x$ in all levels,

$$n_x = \sum_j n_j, \tag{10}$$

and together these equations constitute a complete system that can be solved iteratively.

The rates $R_{ij}$ are expressible in terms of the Einstein $A_{ij}$ and $B_{ij}$ coefficients, and the collisional excitation ($i < j$) and de-excitation ($i > j$) rates $C_{ij}$:

$$R_{ij} = \begin{cases} A_{ij} + B_{ij}\langle J_{ij}\rangle + C_{ij}, & E_i > E_j, \\ B_{ij}\langle J_{ij}\rangle + C_{ij}, & E_i < E_j. \end{cases} \tag{11}$$

The Einstein $A_{ij}$ coefficient gives the rate of an electron decaying radiatively from an upper state $i$ to a lower state $j$. The Einstein $B_{ij}$ rate gives the rate of an atom or molecule absorbing a photon, which causes an electron to be excited from a lower state $j$ to an upper state $i$. The collision rate $C_{ij}$ sets the coupling between the excitation of the atom or molecule and the kinetic energy of the gas and depends (for each collisional partner such as atomic and molecular hydrogen and helium) on the kinetic temperature of the gas. $\langle J_{ij}\rangle$ is the mean integrated radiation field over $4\pi$ sr at a frequency $\nu_{ij}$ corresponding to a transition from level $i$ to $j$ and is given by

$$\langle J_{ij}\rangle = (1 - \beta_{ij})S_{ij} + \beta_{ij} B_{ij}(\nu_{ij}), \tag{12}$$

where $\beta_{ij}$ is the escape probability of a photon and $S_{ij}$ is the source function. The background radiation $B_{ij}(\nu_{ij})$ comes from the infrared emission of dust at a temperature $T_\mathrm{d}$ and the temperature of the CMB $T_\mathrm{CMB}$ at the redshift of interest. The background radiation field is given by

$$B_{ij}(\nu_{ij}) = B(\nu_{ij}, T = T_\mathrm{CMB}) + \tau_\mathrm{d}(\nu_{ij})B(\nu_{ij}, T_\mathrm{d}), \tag{13}$$

where $\tau_\mathrm{d}(\nu_{ij}) = \tau_{100\mu\mathrm{m}}(100\,\mu\mathrm{m}/\lambda)$. We adopt a value of $\tau_{100\mu\mathrm{m}/\lambda} = 0.001$ (Hollenbach, Takahashi & Tielens 1991).

The source function is defined as the ratio between the emission coefficient and the absorption coefficient. It is a measure of how photons in a light beam are absorbed and replaced by new emitted photons by the system it passes through and is given by

$$S_{ij} = \frac{n_j A_{ij}}{n_i B_{ij} - n_j B_{ji}} = \frac{2h\nu_{ij}^3}{c^2}\left[\frac{n_j g_i}{n_i g_j} - 1\right]^{-1}, \tag{14}$$

where $g_i$ and $g_j$ are the statistical weights of level $i$ and $j$, $n_i$ and $n_j$ the population density in the $i$th and $j$th level, $h\nu_{ij}$ is the energy difference between the levels $i$ and $j$, and $c$ the speed of light.

As mentioned above, calculating the emitted intensity by a molecular cloud requires knowledge of the escape probability of the emitted photons. For a sphere, the probability of a photon emitted in the transition from level $i$ to level $j$ to escape the cloud is given by

$$\beta_{ij} = \frac{1 - \exp(-\tau_{ij})}{\tau_{ij}}, \tag{15}$$

where $\tau_{ij}$ is the optical depth in the line. The optical depth in the line over a distance running from $s_1$ to $s_2$ is given by

$$\tau_{ij} = \frac{A_{ij}c^3}{8\pi\nu_{ij}^3}\int_{s_1}^{s_2} \frac{n_i}{\Delta v_\mathrm{d}}\left[\frac{n_j g_i}{n_i g_j} - 1\right] \mathrm{d}s, \tag{16}$$

where $\Delta v_\mathrm{d}$ is the velocity dispersion of the gas due to local turbulence in the cloud.

The emerging specific intensity from a single molecular cloud can now be expressed as

$$\mathrm{d}I_\nu^z = \frac{1}{4\pi} n_i A_{ij} h\nu_{ij}\beta(\tau_{ij})\left(\frac{S_{ij} - B_{ij}(\nu_{ij})}{S_{ij}}\right)\phi(\nu)\mathrm{d}z, \tag{17}$$

where $\mathrm{d}I_\nu^z$ has units of erg cm$^{-2}$ s$^{-1}$ sr$^{-1}$ Hz$^{-1}$, $\phi(\nu)$ is the profile function, which is the Doppler correction to the photon frequency due to local turbulence inside the cloud and large-scale bulk motions, and $B_{ij}(\nu_{ij})$ is the local continuum background radiation at the frequency $\nu_{ij}$.

The sizes of individual molecular clouds in galaxies are often much smaller than the 200 pc resolution of our grid. To account for this we assume that a grid cell is made up by small molecular clouds all with a size of the Jeans length that belongs to the typical temperature and density of the grid cell.

To include the effects of clumping in a molecular cloud, we multiply the collisional rates $C_{ij}$ with a clumping factor $f_\mathrm{cl}$ (Krumholz 2014), the factor by which the mass-weighted mean density exceeds the volume-weighted mean density. In a supersonic turbulent medium this factor can be approximated by

$$f_\mathrm{cl} = \sqrt{1 + 0.75\Delta v_\mathrm{d}^2/c_\mathrm{s}^2}, \tag{18}$$

where $c_\mathrm{s}$ is the sound speed of the medium (e.g. Ostriker, Stone & Gammie 2001; Federrath, Klessen & Schmidt 2008; Lemaster & Stone 2008; Price, Federrath & Brunt 2011).

We assign the individual molecular clouds a relative velocity with respect to each other drawn from a Gaussian distribution centred around 0 km s$^{-1}$, with the velocity dispersion determined for that grid cell as the standard deviation. We calculate the contribution of each of these individual molecular clouds within the sub-grid to the emitted radiation and take the overlap in optical depth space of the molecular clouds into account. This is a fundamental update to the sub-grid treatment of the radiative transfer approach with respect to P14, where the individual molecular clouds had the same relative velocity. We expect the optical depth within a grid cell to be smaller than in P14, effectively allowing more emission to escape from dense regions.

The line intensity escaping the galaxy is computed using a ray-tracing approach, including the effects of kinematic structures in the gas and optical depth effects along the line of sight towards the observer. The emerging specific intensity is dependent on the escape probabilities within a grid cell as well as connecting adjacent grid points along the line of sight. This makes our approach more physical compared to the purely local nature of the Large Velocity Gradient approximation (e.g. Weiß, Walter & Scoville 2005).

Level populations for $^{12}$CO and C$^+$ are calculated using rate coefficients available in the Leiden Atomic and Molecular Database (Schöier et al. 2005). We use $H_2$ and helium as the main

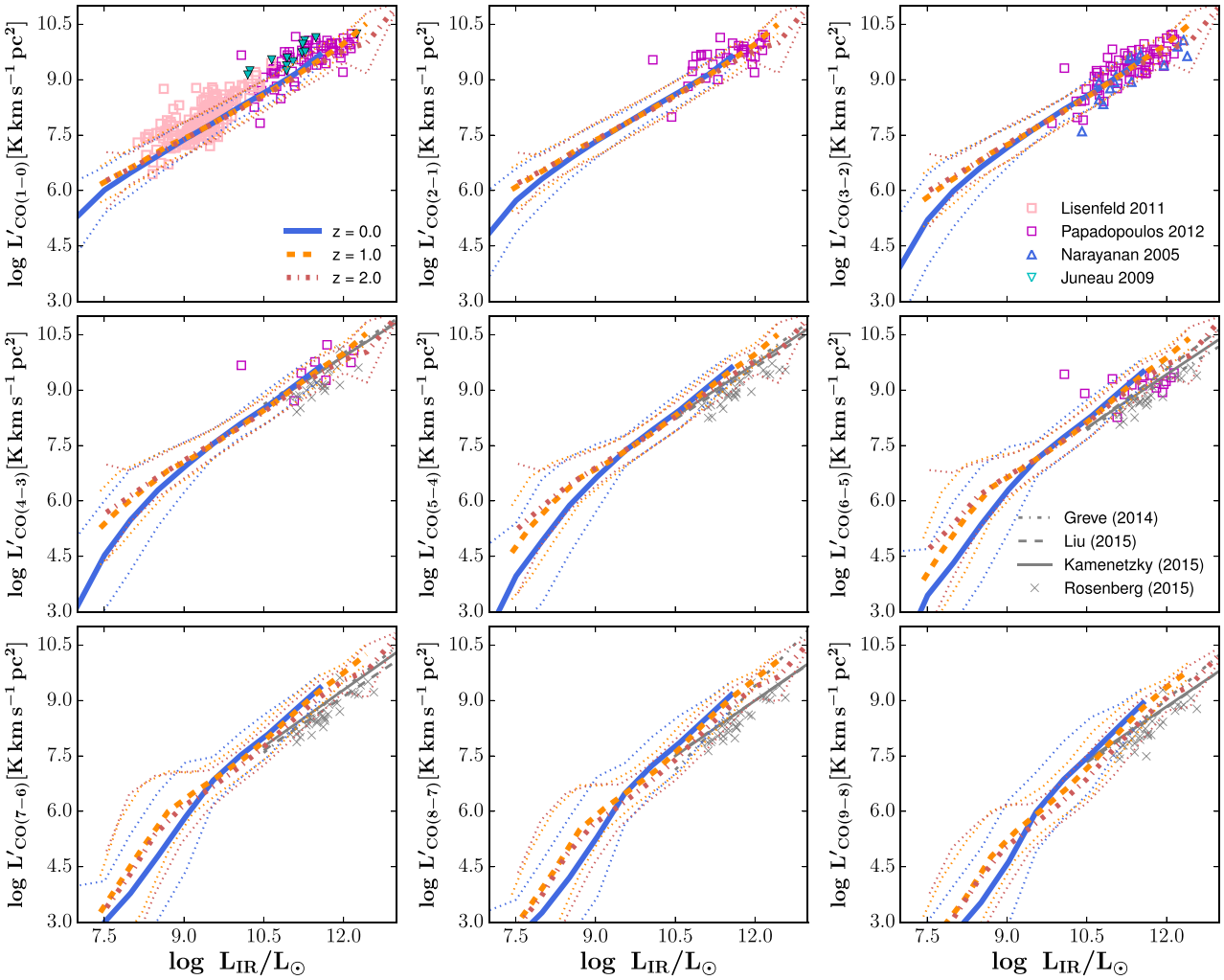


**Figure 2.** CO line-luminosity of CO J = 1–0 up to CO J = 9–8 as a function of FIR luminosity at redshifts $z = 0$, $z = 1$, and $z = 2$. Model results are compared to observations taken from Narayanan et al. (2005), Juneau et al. (2009), Lisenfeld et al. (2011), Papadopoulos et al. (2012), Greve et al. (2014), Liu et al. (2015), Rosenberg et al. (2015), and Kamenetzky et al. (2015). The thick lines show the median of the model predictions, whereas the dotted lines represent the $2\sigma$ deviation from the median.

collision partners for the radiative transfer calculations for CO. The collisional partners for ionized carbon are $H_2$, H I, and an electron abundance that scales with the $C^+$ abundance. The densities of the collisional partners are derived from the galaxy formation model described in Section 2.1.

## 3 CO AND [C II] SCALING RELATIONS

In this section, we present our model predictions for the CO and [C II] line luminosities of galaxies as a function of SFR and IR luminosity. Very similar predictions were shown in P14. In this work, we have significantly updated the recipes for the cooling of gas and the sub-grid treatment of the radiative transfer approach. We therefore believe it is good to reassure ourselves that our model reaches good agreement with observations. Furthermore, in this work, we extend the comparison between model and observations out to CO J = 9–8.

The simulations were run on a grid of haloes with viral masses ranging from $10^9$ up to $5 \times 10^{14}$ $M_\odot$, with a resolution down to $10^7$ $M_\odot$. From these simulations, we selected all central galaxies with a molecular hydrogen gas mass more massive than the mass resolution of our simulations. In this section, we restricted our analysis to central star-forming galaxies, selected using the criterion sSFR $> 1/(3t_H(z))$, where sSFR is the galaxy specific star formation rate and $t_H(z)$ the Hubble time at the galaxy's redshift. This approach selects similar galaxies to commonly used observational methods for selecting star-forming galaxies (e.g. Lang et al. 2014).

Before presenting actual scaling relations, we show normalized distribution functions of the density-weighted average gas density, UV radiation field, gas temperature and dust temperature in the modelled central star-forming galaxies in Fig. 1. This should give the reader a sense of the evolving ISM in the modelled galaxies. We find that the density and radiation field of the ISM in galaxies decrease with cosmic time. Similarly, the average temperatures of dust and gas also decrease with cosmic time. The contribution of the CMB to the temperature of the dust is visible in the lower limit of dust temperatures at $z = 4$ and $z = 6$. We note that these properties are density-weighted averages and can vary between the grid cells within a galaxy.

### 3.1 CO

In Fig. 2, we show the predicted CO J = 1–0 out to CO J = 9–8 line luminosity of galaxies at redshifts $z = 0$, 1, and 2 as a function

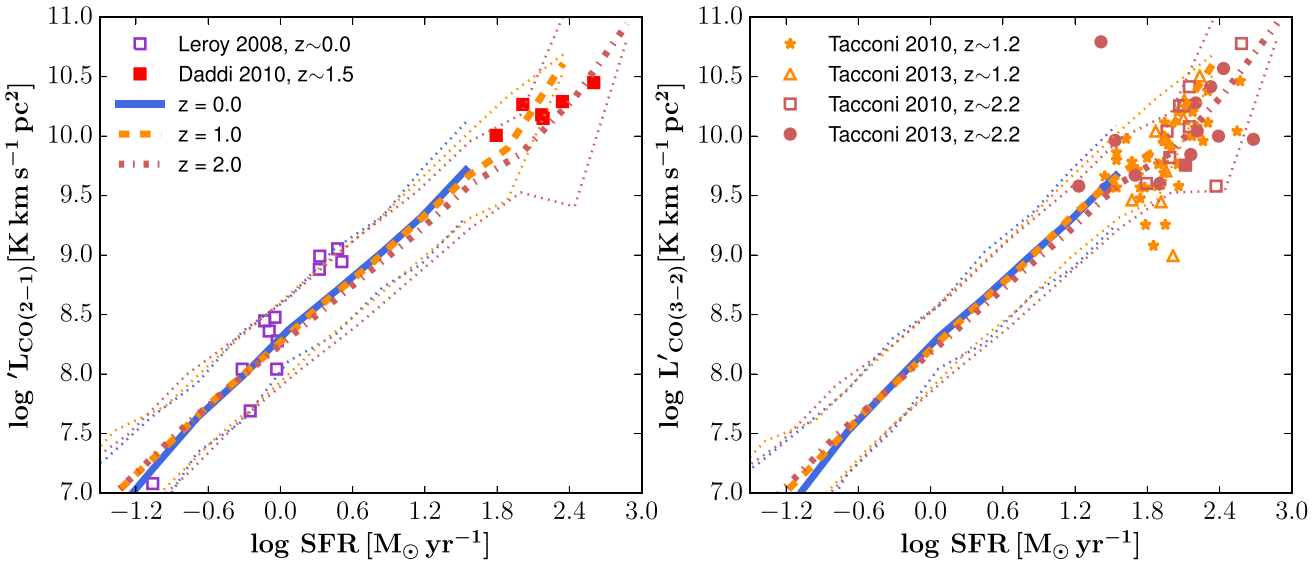


**Figure 3.** CO line luminosity of CO J = 2–1 (left-hand panel) and CO J = 3–2 (right-hand panel) as a function of SFR for modelled galaxies at $z = 0$, $z = 1$, and $z = 2$. Observations are taken from Leroy et al. (2009), Daddi et al. (2010), Tacconi et al. (2010), and Tacconi et al. (2013).

of their FIR luminosity. Our model predictions at $z = 0$ are in good agreement with observational constraints from CO J = 1–0 out to CO J = 5–4. We compare our predictions for the CO J = 4–3 and higher line emission of galaxies with data and fits from the literature Greve et al. (2014); Liu et al. (2015); Rosenberg et al. (2015); Kamenetzky et al. (2015). Our model results are in good agreement with the observations for CO J = 4–3 and CO J = 5–4. We predict slightly too much line emission for the higher CO rotational transitions at $z = 0$ compared with observations. In P14, we predicted too much CO emission for CO J = 2–1 and higher rotational transitions. Overall we find that the agreement between our model and the $z = 0$ observations has improved compared to the P14 results.

We find hardly any time evolution in the relation between FIR luminosity and CO line luminosity for galaxies with FIR luminosities fainter than $\sim 10^{11.5}$ L$_\odot$. We find minor evolution towards FIR brighter galaxies, where the CO luminosity of galaxies decreases with increasing redshifts. This supports a redshift-independent relation between the FIR and CO line luminosity of galaxies. Similar to our $z = 0$ predictions, we predict slightly too much line emission for CO J = 6–5 and higher rotational transitions.

In Fig. 3, we plot the predicted CO J = 2–1 and CO J = 3–2 line emission of galaxies as a function of galaxy SFR at redshift $z = 0$, 1 and 2. We compare our predictions with direct observations of the CO emission lines taken from Leroy et al. (2009), Daddi et al. (2010), Tacconi et al. (2010), and Tacconi et al. (2013). We reach good agreement with the observed CO luminosities at all redshifts.

We find mild evolution in the relation between CO luminosity and SFR towards the galaxies with highest SFRs (SFR$> 15\,M_\odot\,yr^{-1}$), where the CO luminosity of galaxies slightly decreases towards lower redshifts. The rate of this evolution is less than we found in P14. We ascribe that to a better treatment of the sub-grid physics introduced to properly account for optical depth effects within a grid cell. In P14, we did not introduce a local velocity dispersion between the individual molecular clouds in a grid cell. This led to optical depths that were slightly too large, which resulted in an underestimate of the emitted CO radiation in dense (high-redshift) objects. The lack of galaxies at $z = 0$ with SFR $\sim 100\,M_\odot\,yr^{-1}$ is because of the quenching of actively star-forming objects.

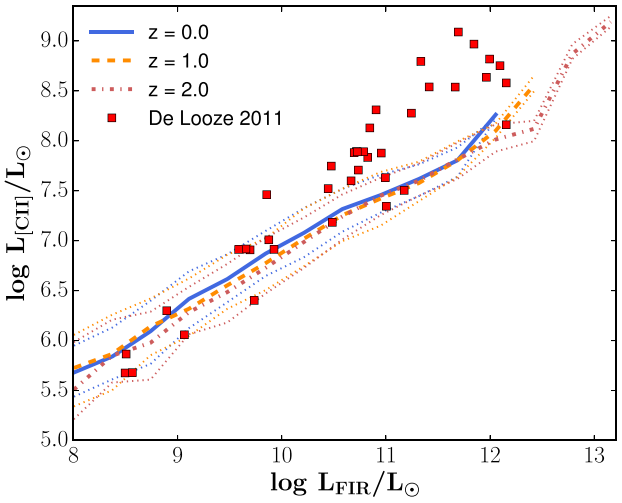


**Figure 4.** Luminosity of the atomic cooling line [C II] (158 μm) as a function of FIR luminosity for galaxies at $z = 0$, $z = 1$, and $z = 2$. Observations at $z = 0$ are from de Looze et al. (2011).

Overall we find that our model is able to reproduce available observations of CO line luminosities very well out to transitions of CO J = 5–4. We predict slightly too much emission towards the highest transitions we explored. In the remainder of this paper, we will focus on CO line transitions ranging from CO J = 1–0 to CO J = 6–5.

### 3.2 [C II]

We plot the [C II] luminosity of galaxies as a function of their FIR luminosity in Fig. 4. We find decent agreement between our model predictions at $z = 0$ and the de Looze et al. (2011) observations of the [C II] luminosity of galaxies at FIR luminosities less than $10^{11}$ L$_\odot$.We underpredict the [C II] luminosity of FIR-brighter galaxies. We find hardly any evolution in the [C II] luminosity of galaxies at fixed FIR luminosity from $z = 0$ to $z = 2$.

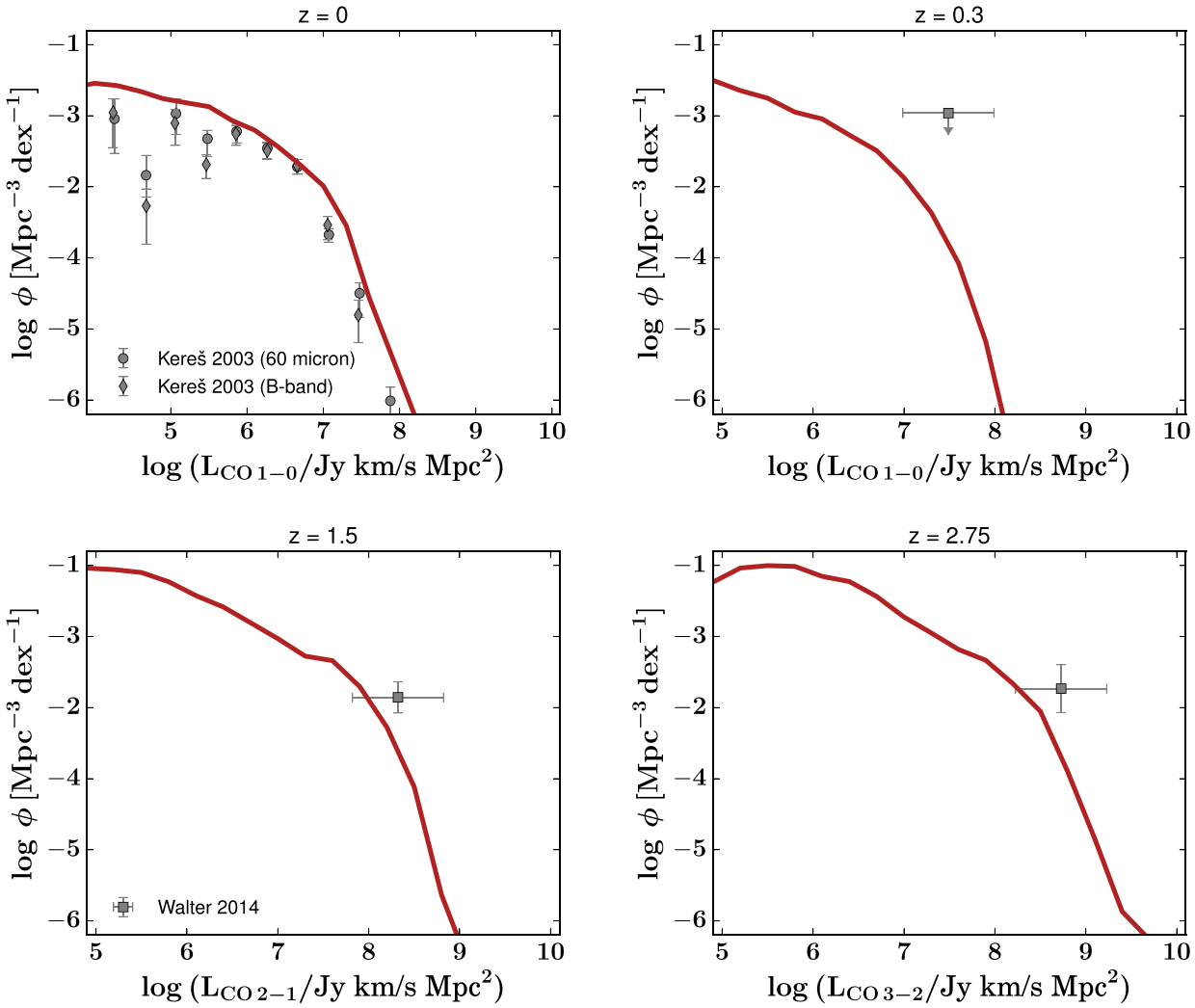


**Figure 5.** Comparison between model predictions and observations of the CO luminosity at $z = 0.0$ (CO J = 1–0; upper left panel), $z = 0.3$ (CO J = 1–0; upper right panel), $z = 1.5$ (CO J = 2–1; lower left panel), and $z = 2.75$ (CO J = 3–2; lower right panel). Predictions are compared to observational constraints from Keres, Yun & Young (2003) and Walter et al. (2014).

## 4 CO AND [C II] LUMINOSITY FUNCTIONS

In this section, we present our predictions for the CO and [C II] luminosity function of galaxies at different redshifts. Unlike in Section 3, we selected all galaxies (both centrals and satellites and selection criteria based on the SFR of galaxies was applied). We first compare our predictions with observational estimates of the CO luminosity function from the literature at different redshifts. We then present predictions for future observations, and focus on the evolution in the shape of the CO luminosity function. We finish by presenting the evolution of the [C II] luminosity function and its shape.

We plot the different CO luminosity functions in terms of the velocity-integrated luminosity $L_{CO}$ with units of Jy km s$^{-1}$ Mpc$^2$, as this gives a better representation through which of the CO J-transitions the dominant CO cooling occurs. These units can easily be converted into commonly used brightness temperature luminosities $L'_{CO}$ in K km s$^{-1}$ pc$^2$ using the equation

$$L'_{CO} = \frac{c^3}{8\pi k_B \nu_{rest}^3} L_{CO}, \quad (19)$$

where $k_B$ is the Boltzmann constant and $\nu_{rest}$ the rest frequency (i.e. not redshifted) of the transition.

### 4.1 Carbon monoxide

#### 4.1.1 *Comparison with the literature*

Fig. 5 shows a comparison between predicted CO luminosity functions and observational constraints from Keres et al. (2003) at $z = 0.0$ and Walter et al. (2014) at $z = 0.3, z = 1.5$, and $z = 2.75$. To avoid including an additional uncertainty in the conversion of high CO J-transitions to CO J = 1–0, we chose to carry out the comparison for the CO J-transitions that were originally observed.

Our model predictions for CO J = 1–0 at $z = 0$ are in good agreement with the observed CO luminosity function by Keres et al. (2003). We slightly overpredict the number of galaxies with CO J = 1–0 luminosities less than $10^5$ Jy km s$^{-1}$ Mpc$^2$, and properly reproduce the number of galaxies with brighter CO luminosities. Our model predictions fall within the uncertainty regions of observational constraints on the CO J = 1–0, J = 2–1, and J = 3–2, luminosity function of galaxies at redshifts $z = 0.3$, $z = 1.5$,

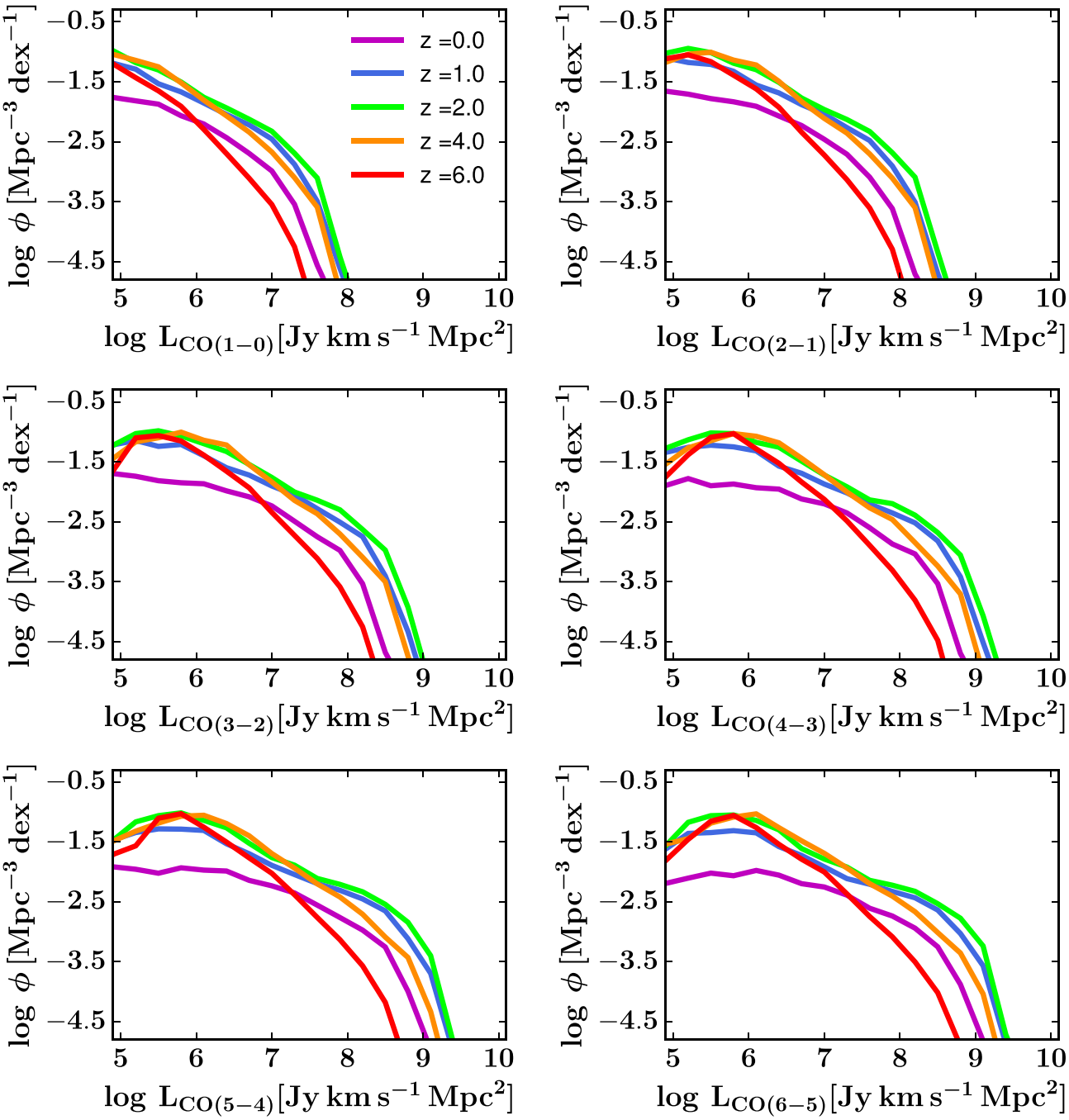


**Figure 6.** Model predictions of the CO J = 1–0 up to the CO J = 6–5 luminosity function of galaxies from $z = 0$ out to $z = 6$.

and $z = 2.75$, respectively. It must be said that our predictions at $z = 1.5$ and especially $z = 2.75$ are only barely in agreement with the available observational constraints. Walter et al. (2014) showed that other models fail to reproduce their observational constraint at $z = 2.75$. We elaborate further on this in Section 5. Unfortunately, there are currently no direct constraints available for the low-mass end of the CO luminosity function at $z > 0$.

### *4.1.2 Evolution of the CO luminosity function*

In this section, we present our predictions for the evolution of CO luminosity functions. It is expected that in the near future more and more deep blind fields and indirect efforts will provide constraints on the CO luminosity function, ultimately probing the molecular hydrogen density of our Universe (through an CO-to-$H_2$ mass conversion factor, see Bolatto, Wolfire & Leroy 2013, for a review)

Fig. 6 shows a clear pattern in the evolution of the luminosity function of different CO J-transitions with time. The number density of galaxies increases from $z = 6$ to $z = 4$ after which the number density stays remarkably constant till $z = 1$. This behaviour holds over the entire luminosity range probed. At $z < 1.0$, the number density decreases over the entire range of CO luminosities, independent of the CO J-transition. This type of evolution (a relatively constant luminosity function at redshifts $z = 1$–4 and decreasing number

**Table 1.** Schechter parameters for the CO J = 1–0 up to J = 6–5 luminosity function from redshift $z = 0$ to $z = 6$.

| Transition | Redshift | $\alpha$ | log $L_*$ (Jy km s$^{-1}$ Mpc$^2$) | log $\phi_*$ (Mpc$^{-3}$ dex$^{-1}$) |
|---|---|---|---|---|
| CO J = 1–0 | 0 | −1.36 | 6.97 | −2.85 |
| CO J = 1–0 | 1 | −1.49 | 7.25 | −2.73 |
| CO J = 1–0 | 2 | −1.52 | 7.30 | −2.63 |
| CO J = 1–0 | 4 | −1.71 | 7.26 | −2.94 |
| CO J = 1–0 | 6 | −1.94 | 6.99 | −3.46 |
| CO J = 2–1 | 0 | −1.35 | 7.54 | −2.85 |
| CO J = 2–1 | 1 | −1.47 | 7.84 | −2.72 |
| CO J = 2–1 | 2 | −1.52 | 7.92 | −2.66 |
| CO J = 2–1 | 4 | −1.75 | 7.89 | −3.00 |
| CO J = 2–1 | 6 | −2.00 | 7.62 | −3.56 |
| CO J = 3–2 | 0 | −1.29 | 7.83 | −2.81 |
| CO J = 3–2 | 1 | −1.47 | 8.23 | −2.79 |
| CO J = 3–2 | 2 | −1.53 | 8.36 | −2.78 |
| CO J = 3–2 | 4 | −1.76 | 8.26 | −3.11 |
| CO J = 3–2 | 6 | −2.00 | 7.95 | −3.60 |
| CO J = 4–3 | 0 | −1.29 | 8.16 | −2.93 |
| CO J = 4–3 | 1 | −1.45 | 8.50 | −2.84 |
| CO J = 4–3 | 2 | −1.51 | 8.64 | −2.85 |
| CO J = 4–3 | 4 | −1.80 | 8.70 | −3.45 |
| CO J = 4–3 | 6 | −2.03 | 8.23 | −3.78 |
| CO J = 5–4 | 0 | −1.20 | 8.37 | −2.94 |
| CO J = 5–4 | 1 | −1.47 | 8.80 | −3.03 |
| CO J = 5–4 | 2 | −1.45 | 8.74 | −2.80 |
| CO J = 5–4 | 4 | −1.76 | 8.73 | −3.34 |
| CO J = 5–4 | 6 | −1.95 | 8.30 | −3.67 |
| CO J = 6–5 | 0 | −1.15 | 8.38 | −2.92 |
| CO J = 6–5 | 1 | −1.41 | 8.74 | −2.92 |
| CO J = 6–5 | 2 | −1.43 | 8.77 | −2.80 |
| CO J = 6–5 | 4 | −1.73 | 8.84 | −3.40 |
| CO J = 6–5 | 6 | −1.93 | 8.38 | −3.72 |

densities at later times) was also seen in the model predictions for the $H_2$ mass function of galaxies (PST14).

#### 4.1.3 Shape of the CO luminosity function

Since the different CO J-transitions trace different phases of the molecular ISM, differences in evolution may hint towards differences in the composition of the ISM in galaxies with time. To better quantify the evolution, we fit our predicted CO luminosity functions with a Schechter function

$$\phi(L_{\rm CO}) = \frac{{\rm d}n}{d\log L_{\rm CO}} = \ln 10\,\phi_* \left(\frac{L_{\rm CO}}{L_*}\right)^{\alpha+1} {\rm e}^{-\frac{L_{\rm CO}}{L_*}}. \quad (20)$$

In this equation, $L_*$ is the luminosity at which the Schechter function turns from a power law into an exponential, $\alpha$ is the slope of the power law, and $\phi_*$ is the normalization of the luminosity function. In the remainder of this work, we will focus on the turning point $L_*$ and the slope of the power-law component $\alpha$, as these two ultimately set the shape of the luminosity function. The fitting results are all presented in Table 1.

We plot the evolution of $L_*$ for CO J = 1–0 out to CO J = 6–5 in Fig. 7. $L_*$ increases from $z = 6$ to $z = 4$–3 for all transitions, after which it gradually decreases to $z = 0$. The evolution in $L_*$ is very minor for CO J = 1–0, ∼0.1–0.2 dex over the entire redshift range probed. CO J = 2–1 and CO J = 3–2 have a similar evolution of up to ∼0.3 dex. The rate of evolution increases towards the higher CO J-transitions, where we find a decrease of 0.5 dex in $L_*$ for CO J = 6–5 from $z = 4$ to $z = 0$.

There is a big difference in the absolute value for $L_*$ for the different CO transitions. Especially CO J = 1–0 has a characteristic luminosity 0.5 dex less than CO J = 2–1 and almost a full dex and even more for CO J = 3–2 and higher transitions, respectively.

The right-hand panel of Fig. 7 shows the evolution of the power-law slope $\alpha$ for the six different CO J-transitions. We find a general trend where the slope becomes shallower towards lower redshifts. We will further discuss these results in Section 5.

The faint end of the CO luminosity functions evolve differently for the respective rotational transitions. We predict less evolution in the faint end of the CO J = 1–0 luminosity function than in the faint end of for example the CO J = 4–3 luminosity function. To understand this different evolution, we plot the $H_2$-to-CO ratio (the ratio between molecular hydrogen mass and the velocity-integrated CO luminosity) as a function of CO luminosity for the different rotational transitions in Fig. 8. In general, we find that the $H_2$-to-CO ratio decreases with increasing redshift (i.e. the same CO luminosity traces a smaller $H_2$ mass towards higher redshifts). Furthermore, we find that the $H_2$-to-CO ratio decreases as a function of CO luminosity. This decline is stronger for high rotational J-transitions. A close look at the $H_2$-to-CO ratios reveals that at CO luminosities of $\sim 10^6$ Jy km s$^{-1}$ Mpc$^2$ the ratio between $H_2$ mass and CO J = 1–0 luminosity evolves with only a factor of ∼2 from redshift $z = 6$ to $z = 0$, whereas the ratio between $H_2$ mass and CO J = 6–5 decreases almost four times from $z = 6$ to $z = 0$.

We will discuss how the changing ratio between CO luminosity and $H_2$ mass shapes the CO luminosity functions in Section 5. The predicted turnover at low luminosities for luminosity functions of CO rotational transitions J = 3–2 and higher at redshifts $z > 2$ is due to resolution.

### 4.2 [C II] luminosity function

In Fig. 9, we show the evolution of the [C II] luminosity function of galaxies from redshift $z = 0$ out to $z = 6$. We find a strong evolution in the [C II] luminosity function with time. We find an increase in the number densities from $z = 6$ to $z = 4$. The number densities remain relatively constant from $z = 4$ to $z = 2$, and decrease again towards lower redshifts. This behaviour is again similar to our predictions for the CO luminosity functions and our predictions for the $H_2$ mass functions (PST14), indicative that our predicted [C II] luminosity function is driven by the same physical processes.

We compare our predictions with the lower limit set by Swinbank et al. (2012) based on [C II] observations of two galaxies at redshift $z$ ∼ 4.4. We find that our predictions for the [C II] luminosity function at $z = 4$ is below the lower limit found by Swinbank et al. (2012). This suggests that our model does not predict enough [C II]-bright galaxies at these redshifts. This is similar to our predictions for the CO luminosity function at $z = 2.75$, where we barely predicted enough CO bright objects. We will further discuss the match with the Swinbank et al. lower limit in Section 5.

We present the evolution in the parameters $L_*$[C II] and $\alpha$ of the Schechter function fit to the [C II] luminosity function in Fig. 10 and in Table 2. We find that $L_*$[C II] is relatively constant from $z = 6$ to $z = 2$, and rapidly decreases at lower redshifts. The rapid drop in $L_*$[C II] at redshifts $z < 2$ strongly resembles the evolution of the cosmic SFR density of the Universe, driven by the strong connection between SFR and [C II] luminosity in our model. $\alpha$ increases from $z = 6$ to $z = 4$, then remains relatively constant out to $z = 1.0$, and increases again at later times.

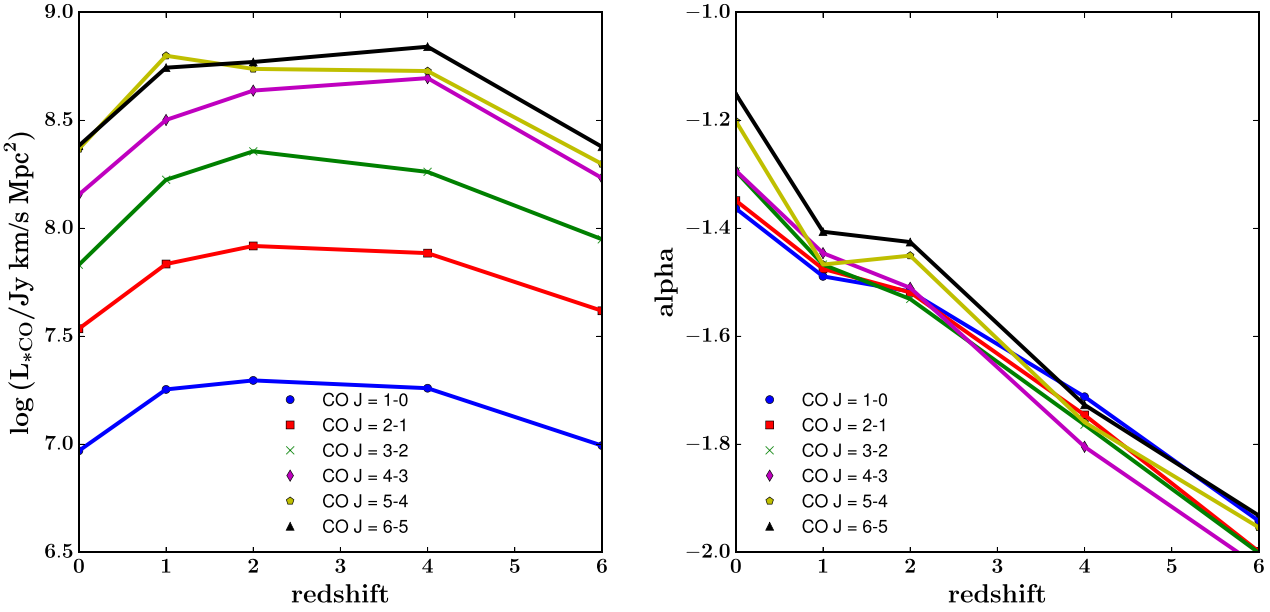


**Figure 7.** Evolution of the turning point of the Schechter function $L_*$ (left) and the slope of the power-law component of the Schechter function $\alpha$ (right) for predicted CO luminosity function from CO J = 1–0 up to CO J = 6–5 from redshift $z = 6$ to $z = 0$.

## 5 DISCUSSION

### 5.1 Observing CO deep fields

The presented model predictions can be a very valuable asset for future observing proposals. In Table 3, we show how much time it requires to detect the knee of the different CO luminosity functions at our redshifts of interest over 1 arcmin$^2$ on the sky (the survey speed). Where observable, we performed the calculations for ALMA (50 12 m antennas), the JVLA, and the ngVLA (assuming dishes of 18 m). We required a 5$\sigma$ detection of the knee of the luminosity function (as given in Table 1) and a spectral resolution of 300 km s$^{-1}$. The reader can use this as a starting point and easily recalculate the survey speeds for smaller or larger areas or a different requested sensitivity. The table only takes time on source into account and one should be aware of additional overheads.

We immediately notice that the required observing times vary significantly. In some cases, observing the knee of the luminosity function with the current instruments only requires a modest integration time of a few minutes, whereas in other cases it is an exercise that can easily take up tens of hours. A survey focusing on the CO J = 1–0 emission line is much more expensive than surveys focusing on the higher transitions. This is driven by the strong difference in characteristic luminosity $L_*$ for CO J=1–0 with respect to the other transitions (see Fig. 7).

The CO J =3–2 line is the most favourable transition to observe the global gas content of galaxies in a deep-field survey during the peak of SF of our Universe. Its survey speed at redshifts $z \leq 4$ is much shorter than the survey speeds of the CO J = 1–0 and CO J = 2–1 lines. The characteristic density ($\sim 10^{4.5}$ cm$^{-3}$) of the CO J = 3–2 line can still be associated with the bulk molecular gas in a galaxy, which make it more suitable to observe the molecular reservoir of galaxies than higher rotational CO lines with higher survey speeds.

Though the limited field of view of ALMA does not make it an ideal survey instrument, its sensitivity allows one to observe the knee of CO luminosity functions for high CO rotational transitions at $z = 2$ in $\sim$10 h over an area as big as the *Hubble Ultra Deep Field*.

Radio instruments also have the potential to probe the CO luminosity function of galaxies at redshifts $z > 1$, depending on the exact frequency tunings. The radio regime will become very interesting for objects towards redshifts of $z > 3$, where the CO J=3–2 emission line moves out of the currently available ALMA bands. Our results show that the ngVLA will be much more suitable to carry out surveys of sub-mm emission lines than the current JVLA. In some cases, the ngVLA is very complementary to ALMA (e.g. to observe CO J = 1–0 and CO J = 2–1 at $z > 2$) and in other cases, the ngVLA is even more suitable to observe CO luminosity functions (e.g. the CO J=1–0 luminosity function at $z = 2$ and the CO J = 2–1 luminosity function at $z = 6$). The next generation of radio telescopes (Square Kilometer Array and its pathfinders Australian Square Kilometre Array Pathfinder and Karoo Array Telescope) have a very high sensitivity and large field of view compared with ALMA. If these instruments are equipped with a high-frequency receiver (targeting frequencies between 1 and 50 GHz), they will be very efficient carrying out deep fields of low CO J-transitions at redshifts $z > 2$. In the near future, the ngVLA is the most obvious telescope to probe low CO rotational transitions beyond redshifts of $\sim$2.

We encourage the reader to look for the most favourable frequency setting when designing a deep-field survey, rather than just focusing on one CO luminosity function at one particular redshift. With a clever frequency setting, a limited number of tunings can already probe a number of different CO luminosity functions at different redshifts (e.g. Decarli et al. 2014b; Walter et al. 2014).

We want to finish this sub-section with a word of caution. Due to the large difference in rest-frame frequency of the respective CO J-transitions, current estimates of the CO luminosity function are based on different CO J-transitions at different redshifts (Walter et al. 2014, uses CO J = 1–0 at $z = 0.0$ and $z = 0.3$, CO J= 2–1 at $z = 1.5$, and CO J = 3–2 at $z = 2.75$). If the goal of a project is to obtain molecular gas masses, care should be taken to translate luminosity functions of CO into a CO J = 1–0 luminosity function.

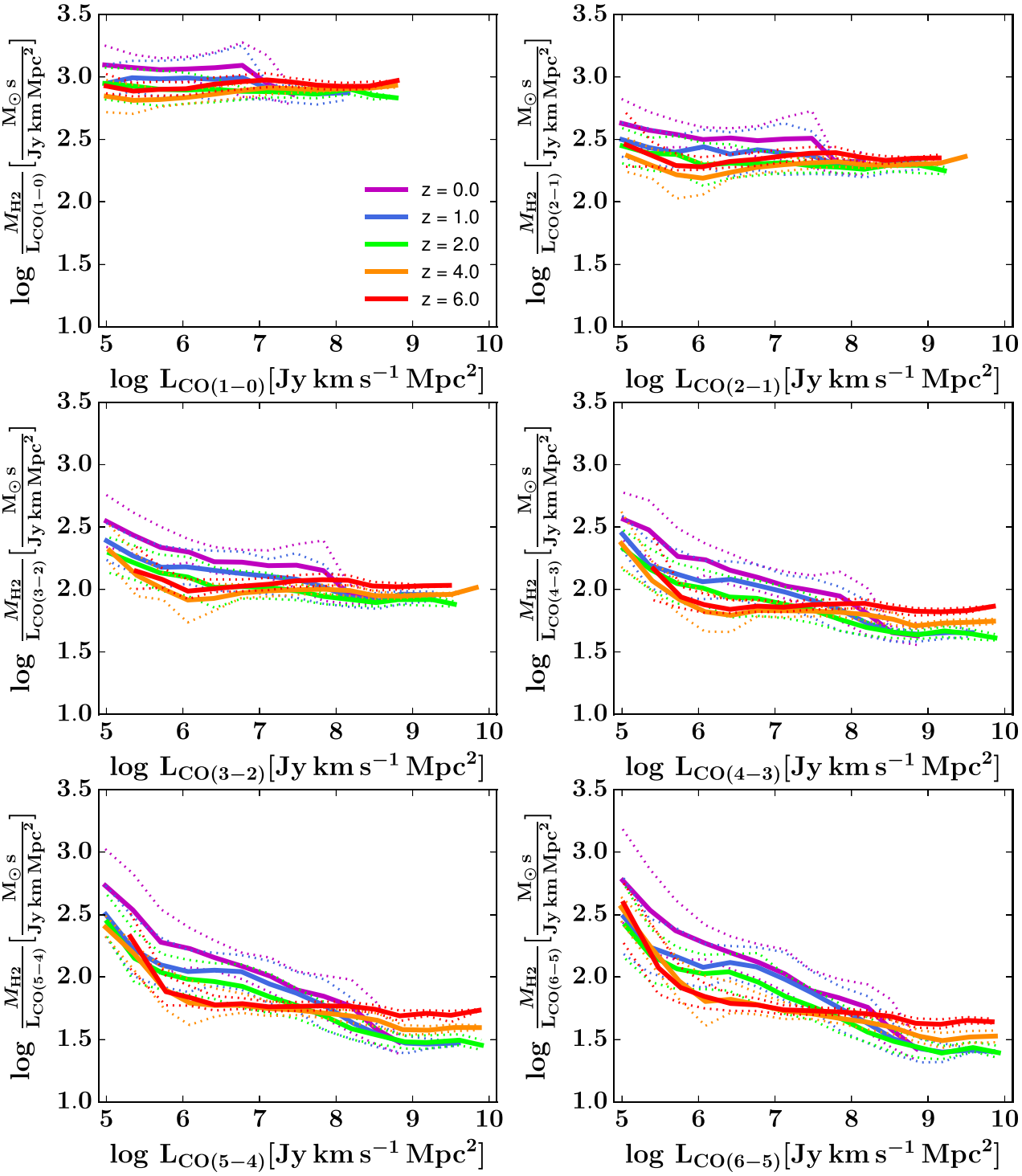


**Figure 8.** The ratio between $H_2$ mass and CO luminosity for CO J = 1–0 up to CO J = 6–5 at redshifts $z = 0$ to $z = 6$. The solid lines show the median of the model predictions, whereas the dotted lines represent the $2\sigma$ deviation from the median. Note the increase in the $H_2$-to-CO ratio at low luminosities with increasing redshift, especially for the higher rotational CO transitions.

Typically, values of 3.2 and 4.5 are assumed for the flux ratio between CO J = 2–1 and CO J = 3–2, and CO J = 1–0, respectively (e.g. Daddi et al. 2015; Dannerbauer et al. 2009, corresponding to brightness temperature luminosity ratios of $L'_{CO2-1}/L'_{CO1-0} = 0.8$, and $L'_{CO3-2}/L'_{CO1-0} = 0.5$). In Fig. 11, we plot the ratio between the characteristic flux density $L_*$ for the CO J = 2–1 and CO J = 3–2 transitions and CO J = 1–0. At $z = 0$, our predictions for the flux ratio are close to the typically adopted ratios for CO J = 2–1, and higher for CO J = 3–2. Our predicted ratio between CO J = 2–1 and CO J =1–0 remains relatively constant with time. The ratio between CO J=3–2 and CO J=1–0 increases towards higher redshifts and decreases again at redshifts $z > 4$. This is driven by changing ISM

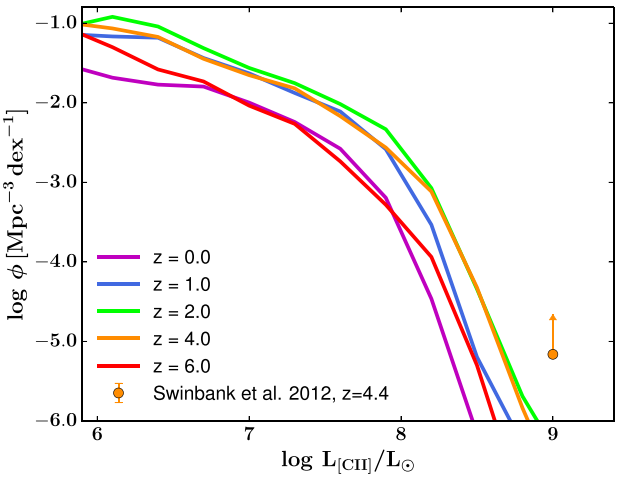


**Figure 9.** Model predictions of the [C II] luminosity function of galaxies from $z = 0$ out to $z = 6$. A lower limit on the [C II] luminosity function at $z = 4.4$ is included from Swinbank et al. (2012).

conditions in galaxies towards higher redshift (see Fig. 1), resulting in a larger CO line ratio (e.g. P14; Narayanan & Krumholz 2014). Moreover, heating of the gas by the CMB at high redshifts can affect the CO line ratios in galaxies with low SFRs (Narayanan & Krumholz 2014). Line ratios can furthermore increase due to the J = 1–0 line losing contrast with respect to the CMB background (da Cunha et al. 2013; Tunnard & Greve 2016).

Without properly accounting for changes in line ratios, the number of galaxies that are bright in CO J = 1–0 will be overestimated. This may eventually lead to an incorrect $H_2$ mass function and an overestimate of the density of molecular hydrogen in our Universe.

### 5.2 Evolution in the shape of the CO luminosity functions

Our predictions show that the rate of evolution for the characteristic luminosity $L_*$ is larger for the high CO J-transitions than for the lower J-transitions (evolution of ∼0.1 dex for CO J=1–0, whereas CO J =6–5 evolves with more than ∼0.5 dex). This indicates that not only the predicted amount of total cooling through CO changes, but also the way this is divided over the different CO transitions. The notion that less cooling occurs through the higher CO rotational transitions indicates that the CO bright galaxies also change their ISM properties, i.e. their ISM consists of a relatively smaller component of dense and warm gas. This is in good agreement with previous predictions made by our models, which showed that as a function of time the CO spectral line energy distribution (SLED) of galaxies peaks towards lower CO rotational transitions (from redshift $z = 2.2$ to redshifts $z = 1.2$, and $z = 0.0$; P14). Daddi et al. (2015) demonstrated that the CO SLEDs of two main-sequence galaxies at $z = 1.5$ have an important CO J = 5–4 component not seen in local main-sequence galaxies. This component is also indicative of clumps of denser and warmer gas in the star-forming ISM of galaxies at $z = 1.5$.

We cannot fail to notice that our models predict the highest number densities of very bright CO objects at redshifts $z = 2$–3. This coincides with the predicted peak in the cold gas and $H_2$ cosmic density (PST14) and the SFR density of our Universe (SPT15). Within our model, the latter is a natural consequence of the former. A high number density of CO bright objects is associated with many $H_2$-rich galaxies. Assuming a molecular-gas-based SF relation, this automatically yields a high SFR density.

**Table 2.** Schechter parameters for the [C II] luminosity function from redshift $z = 0$ to $z = 6$.

| Transition | Redshift | $\alpha$ | log $L_*$ ($L_\odot$) | log $\phi_*$ (Mpc$^{-3}$ dex$^{-1}$) |
|---|---|---|---|---|
| [C II] | 0 | −1.25 | 7.47 | −2.33 |
| [C II] | 1 | −1.43 | 7.66 | −2.15 |
| [C II] | 2 | −1.52 | 7.81 | −2.20 |
| [C II] | 3 | −1.41 | 7.80 | −2.12 |
| [C II] | 4 | −1.53 | 7.85 | −2.37 |
| [C II] | 6 | −1.77 | 7.80 | −2.95 |

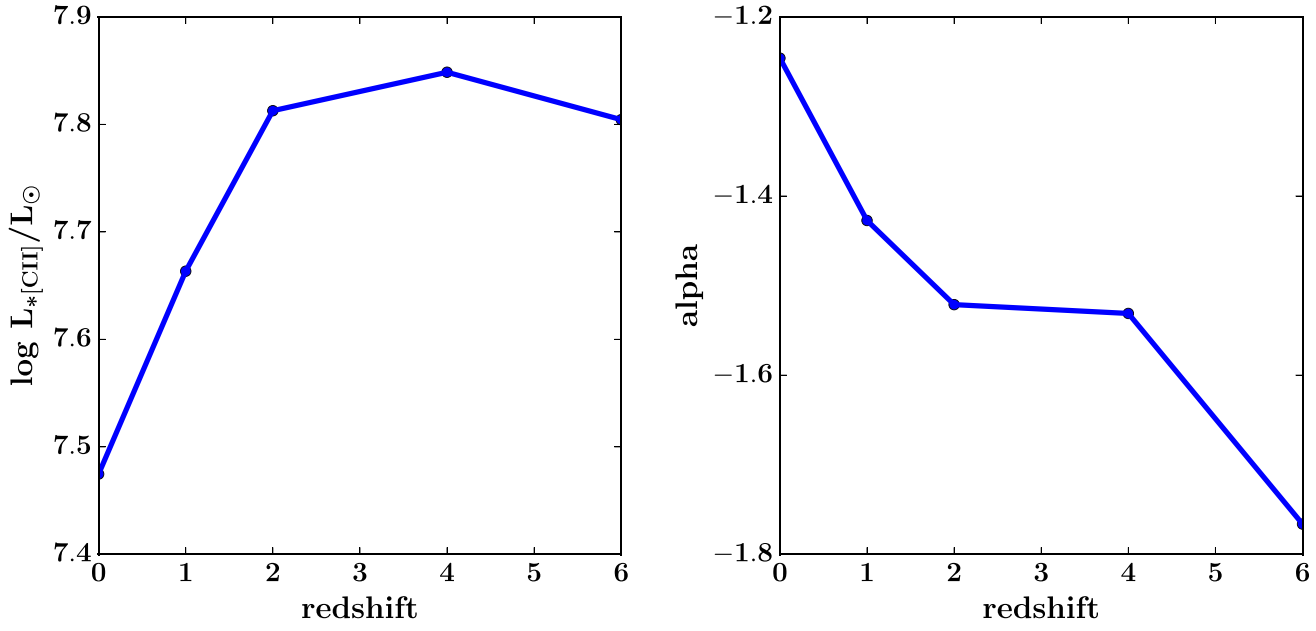


**Figure 10.** Evolution of the turning point of the Schechter function $L_*$ (left) and the slope of the power-law component of the Schechter function $\alpha$ (right) for the predicted [C II] luminosity function from redshift $z = 6$ to $z = 0$.

**Table 3.** Survey speed to observe the knee of the CO luminosity function for CO J = 1–0 up to J = 6–5 over 1 deg$^2$ on the sky with a 5$\sigma$ certainty from redshift $z = 0$ to $z = 6$ using ALMA, the JVLA, and the ngVLA. In some cases, the line is not observable by any of the instrument, in which case the required instruments and survey speed are marked with n/a.

| Transition | Redshift | Observed frequency (GHz) | Instrument | rms/pointing (mJy) | Survey speed (h/arcmin$^2$) |
|---|---|---|---|---|---|
| CO J = 1–0 | 0 | 115.22 | ALMA band 3 | $5 \times 10^5$ | 0.03 |
| CO J = 1–0 | 1 | 67.64 | ALMA band 2 | 0.042 | 44.24 |
| CO J = 1–0 | 2 | 38.42 | ALMA band 1 | 0.013 | 20.51 |
| CO J =1–0 | 2 | 38.42 | JVLA Ka | 0.013 | 90.00 |
| CO J =1–0 | 2 | 38.42 | ngVLA Ka | 0.013 | 18.00 |
| CO J =1–0 | 4 | 23.05 | JVLA K | 0.0036 | 239.18 |
| CO J =1–0 | 4 | 23.05 | ngVLA K | 0.0036 | 47.83 |
| CO J =1–0 | 6 | 16.47 | JVLA Ku | 0.0014 | 341.96 |
| CO J =1–0 | 6 | 16.47 | ngVLA Ku | 0.0014 | 68.39 |
| CO J =2–1 | 0 | 230.54 | ALMA band 6 | $2 \times 10^6$ | 0.12 |
| CO J =2–1 | 1 | 115.26 | ALMA band 3 | 0.165 | 4.9 |
| CO J =2–1 | 2 | 76.85 | ALMA band 2 | 0.053 | 6.22 |
| CO J =2–1 | 4 | 46.11 | JVLA Q | 0.0153 | 132.84 |
| CO J =2–1 | 4 | 46.11 | ngVLA Q | 0.0153 | 26.57 |
| CO J =2–1 | 6 | 32.93 | ALMA band 1 | 0.0044 | 130.54 |
| CO J =2–1 | 6 | 32.93 | JVLA Ka | 0.0044 | 223.5 |
| CO J =2–1 | 6 | 32.93 | ngVLA Ka | 0.0044 | 44.70 |
| CO J =3–2 | 0 | 345.8 | ALMA band 7 | $4 \times 10^6$ | 0.27 |
| CO J =3–2 | 1 | 172.9 | ALMA band 5 | 0.201 | 0.73 |
| CO J =3–2 | 2 | 115.26 | ALMA band 3 | 0.146 | 6.16 |
| CO J =3–2 | 4 | 69.16 | ALMA band 2 | 0.036 | 28.75 |
| CO J =3–2 | 6 | 49.4 | JVLA Q | 0.0095 | 3345.33 |
| CO J =3–2 | 6 | 49.4 | ngVLA Q | 0.0095 | 669.01 |
| CO J =4–3 | 0 | 461.04 | ALMA band 8 | $7 \times 10^6$ | 0.49 |
| CO J =4–3 | 1 | 230.52 | ALMA band 6 | 0.750 | 0.21 |
| CO J =4–3 | 2 | 153.68 | ALMA band 4 | 0.278 | 0.74 |
| CO J =4–3 | 4 | 92.21 | ALMA band 3 | 0.099 | 2.95 |
| CO J =4–3 | 6 | 65.86 | n/a | 0.018 | n/a |
| CO J =5–4 | 0 | 576.27 | n/a | $10^7$ | n/a |
| CO J =5–4 | 1 | 288.13 | ALMA band 7 | 1.50 | 0.19 |
| CO J =5–4 | 2 | 192.09 | ALMA band 5 | 0.35 | 1.16 |
| CO J =5–4 | 4 | 115.25 | ALMA band 3 | 0.106 | 11.66 |
| CO J =5–4 | 6 | 82.32 | ALMA band 2 | 0.0212 | 36.73 |
| CO J =6–5 | 0 | 691.47 | ALMA band 9 | $10^7$ | 1.09 |
| CO J =6–5 | 1 | 345.74 | ALMA band 7 | 1.304 | 0.27 |
| CO J =6–5 | 2 | 230.49 | ALMA band 6 | 0.375 | 0.85 |
| CO J =6–5 | 4 | 138.29 | ALMA band 4 | 0.137 | 2.91 |
| CO J =6–5 | 6 | 98.78 | ALMA band 3 | 0.0026 | 49.88 |

In Fig. 6, we showed that the shape of the CO luminosity function evolves less with redshift for low rotational transitions than for higher rotational transitions. We also showed that at fixed CO luminosity the $H_2$-to-CO ratio of galaxies decreases. The evolution in the $H_2$-to-CO of galaxies is stronger for the higher than the lower rotational transitions. If a fixed CO luminosity traces a smaller $H_2$ reservoir at high redshift, the volume density that belongs to that CO luminosity reservoir will be higher, just because of the slope of the $H_2$ mass function. The evolution in the $H_2$-to-CO ratio is much stronger for the high rotational transitions than for low transitions. Therefore, there will be a stronger evolution in the volume densities for high rotational CO transitions than for low rotational transitions at the faint end of the luminosity function.

These results clearly show that any evolution in the CO luminosity functions is not just driven by an evolution in the gas mass, but also by evolution in the characteristic properties of the ISM that define the shape of the CO SLEDs as seen in Fig. 1. Furthermore, the CMB may also influence the shape and evolution of the CO luminosity function. Background emission from the CMB can affect the CO luminosity functions towards higher redshifts, especially the low CO rotational transitions (Obreschkow & Rawlings 2009; da Cunha et al. 2013; Tunnard & Greve 2016). Additional heating of low-temperature gas by the CMB can slightly increase the excitation conditions and measured CO intensities (Narayanan & Krumholz 2014).

### 5.3 Too few CO-bright galaxies at $z > 2$

We found that our model is barely able to reproduce observational constraints on the CO J = 3–2 luminosity function at $z = 2.75$ from the CO blind survey presented in Walter et al. (2014, Fig. 5). Walter et al. showed that a comparison with other semi-analytic models (Obreschkow et al. 2009; Lagos et al. 2012) yields similar results. We note that the uncertainties on the Walter et al. (2014) results are

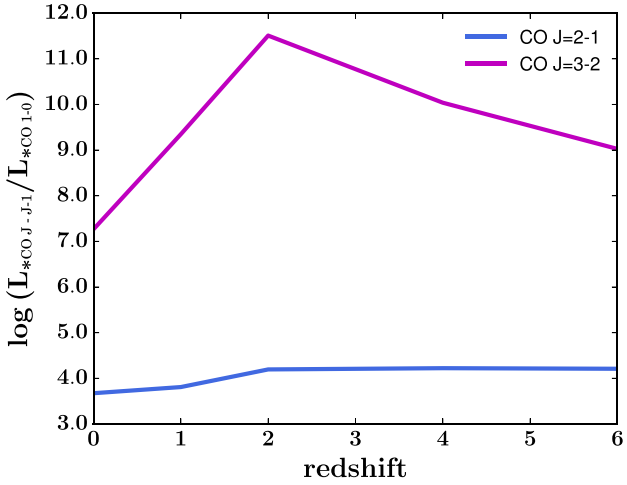


**Figure 11.** The ratio between the characteristic flux density $L_*$ for CO J = 2–1 (blue) and CO J = 3–2 (magenta), and CO J = 1–0 as a function of redshift.

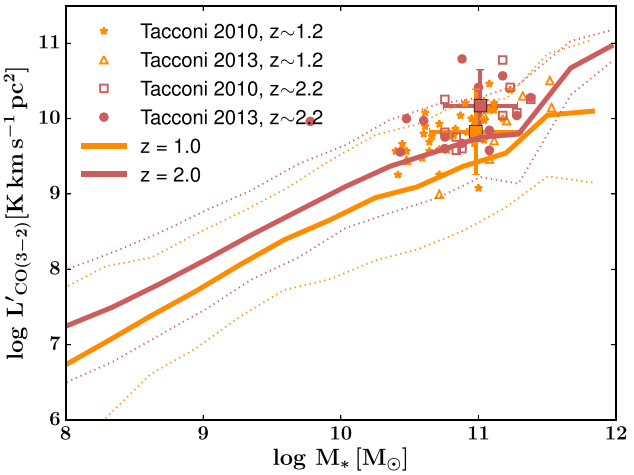


**Figure 12.** CO J =3–2 luminosity of galaxies as a function of their stellar mass at $z = 1$ and $z = 2$. Observations are taken from Tacconi et al. (2010, 2013). Large squares with the black edges mark the mean CO luminosities at redshift $z = 1.2$ and $z = 2.2$ for the combined samples, respectively.

significant. The number of detections is very limited, and the area on the sky probed very small. Effects of cosmic variance may have significant influences on the derived CO number densities.

Vallini et al. (2016) obtained indirect estimates of the CO luminosity function by applying various FIR-to-CO conversions on Herschel data. When comparing their empirical estimates of the CO luminosity function to model predictions, Vallini et al. also found that theoretical models predict too few CO-bright galaxies at $z = 2$. Looking at these results, a picture emerges where at $z \geq 1.5$ theoretical models predict hardly enough CO-bright objects.

To further narrow down what could cause the mismatch between our predictions and the Walter et al. (2014) constraints at $z = 1.5$ and $z = 2.75$, we plot the CO J = 3–2 luminosity of galaxies as a function of stellar mass at $z = 1$ and $z = 2$ in Fig. 12. We compare our predictions with observations taken from Tacconi et al. (2010) and Tacconi et al. (2013) and apply the same selection criteria to our model galaxies.[2] We indeed find that our model predictions for the CO J = 3–2 luminosity of galaxies is ∼0.3 dex too low at a given stellar mass, which could explain the tension between our model predictions and observational constraints of the CO luminosity function. The semi-analytic model used in this work matches the observed stellar mass function at these redshift and at this mass regime quite well (SPT15), but the faint CO luminosities result in a CO luminosity function in poor agreement with observations.

To understand the origin of the mismatch between the predicted and observed CO luminosity function, we need to take a step back and focus on the predicted $H_2$ mass in galaxies. If we naively assume a constant CO J = 3–2/CO J = 1–0 ratio and CO-to-$H_2$ conversion factor, an underestimation of the CO luminosity of galaxies by ∼0.3 dex will result in an underestimation of the molecular gas reservoirs of galaxies of 0.3 dex. Popping, Behroozi & Peeples (2015a) extended a sub-halo abundance matching model with recipes to obtain observationally driven H I and $H_2$ masses of galaxies. They demonstrated that semi-analytic models that include detailed tracking of atomic and molecular hydrogen predict ∼0.3 dex too little cold gas and $H_2$ in star-forming galaxies at $z \sim 2$–3. Popping et al. (2015b) inferred the cold gas (H I + $H_2$), H I, and $H_2$ gas masses of galaxies taken from the Cosmic Assembly Near-infrared Deep Extragalactic Legacy Survey (Grogin et al. 2011; Koekemoer et al. 2011) survey and also found that theoretical models predict ∼0.3 dex too little $H_2$ in galaxies at redshifts $z = 1$–3. A lack of molecular hydrogen translates into galaxy SFRs that are too low at intermediate redshifts. Indeed, theoretical models predict ∼0.3 dex too little SF in galaxies at $z \sim 2$ with stellar masses $> 10^9\,M_\odot$ (Somerville & Davé 2015). If all other properties of galaxies (stellar mass function, fraction of star-forming versus quiescent galaxies) are reproduced, too little $H_2$ will result in an $H_2$ mass function and CO luminosity function in poor agreement with observations. If theoretical models could reproduce the SFRs of galaxies correctly, presumably the CO line luminosities would be correct as well.

Somerville & Davé (2015) showed that most semi-analytic and hydrodynamic models fail to reproduce the massive end of the stellar mass function of galaxies at $z \sim 2$–3 and predict too few massive galaxies (although models that assume that SF efficiency increases towards high-molecular surface density do much better, SPT15). This naturally affects the predicted $H_2$ mass function and CO luminosity function as well.

The mismatch between predicted CO luminosity function and observations does not seem to be related to our modelling of the connection between $H_2$ and line emission, but to be part of a much larger set of problems affecting the SFRs and stellar mass growth in galaxies as well. The results presented in this work are merely a different representation of this problem, and suggest that too small gas reservoirs (both molecular as the combination of molecular and atomic gas) may be at the core of the overall problem. The root of the problem is in the accretion rate of new gas, which is modified by outflows and re-accreting gas. So-called bathtub models have demonstrated the importance of properly accounting for these competing physical processes (Davé, Finlator & Oppenheimer 2012; Mitra, Davé & Finlator 2015), Recent work by White, Somerville & Ferguson (2015) showed that extending the time for ejected gas to re-accrete on to galaxies leads to galaxy gas masses in better agreement with indirect estimates, and improves the match between

[2] Tacconi et al. (2010) and Tacconi et al. (2013) only selected galaxies with SFR $> 30\,M_\odot\,yr^{-1}$.

predicted and observed SFRs and stellar mass functions (see also Henriques et al. 2015).

Given the uncertainties discussed above, it is good to ask ourselves the question how far off the models are from reality and how this affects our predictions. Galaxy formation models typically reproduce the knee of the stellar mass function (Somerville & Davé 2015). We therefore do not expect that our predictions will change much near the knee of the CO luminosity functions. Galaxy formation models typically predict too few galaxies with stellar masses more massive than the knee of the stellar mass function. We can thus expect a higher number of galaxies with CO luminosities brighter than the knee of the respective CO luminosity functions. We showed that our model predicts CO J = 2–1 and CO J = 3–2 luminosities that are ∼0.3 dex too faint compared to observations (Fig. 12) consistent with the low SFRs galaxy formation models predict. If indeed CO luminosities are ∼0.3 dex brighter than suggested by our models, our predicted CO luminosity functions up to CO J = 3–2 should be shifted to brighter values by ∼0.3 dex. Combined with the shape of the luminosity functions, these corrections would shorten the survey speeds mentioned in Tabel 3 and ease the observation of the bright end of CO luminosity functions. It is harder to estimate how our model uncertainties affect the CO luminosity function of the higher CO rotational transitions, as excitation physics play a key role. Nevertheless, we expect that a similar trend holds.

### 5.4 The [C II] luminosity function

We found that the [C II] luminosity function remains constant from $z = 4$ to $z = 2$, after which the number density of the bright [C II] galaxies decreases. To quantify this we showed that $L_{*[\mathrm{C\,II}]}$, the turning point between the power-law and exponential component of the Schechter fit to the [C II] luminosity function, decreases by almost 0.5 dex from $z = 2$ to $z = 0$. This behaviour is remarkably consistent with the evolution of the CO luminosity functions presented in this work and coincides with the predicted peak in the SFR density of our Universe. It also follows earlier predictions for the $H_2$ mass function of galaxies (PST14). This indicates that these different lines and components are closely correlated. This is not necessarily surprising. We only account for the contribution by photodissociation regions (PDRs) to the [C II] luminosity of galaxies. These are the same regions that are responsible for the CO emission and where molecular hydrogen can form. In reality, the ionization of diffuse atomic gas by young stars can also contribute to the [C II] emission from a galaxy. We will further discuss this in Section 5.5.

We found that our predictions for the [C II] luminosity function at $z = 4$ are somewhat lower than the lower limits derived by Swinbank et al. (2012). The lower limits set by Swinbank et al. (2012) were based on [C II] detections of two galaxies, that were serendipitously detected as part of a targeted continuum survey on IR-bright galaxies within a region of 0.25 deg$^2$. Due to the selection bias and serendipitous nature of the detections, the Swinbank et al. survey may overestimate the number density of [C II]-bright sources per unit volume. This could explain some of the discrepancy between the lower limits set in Swinbank et al. (2012) and our work.

Matsuda et al. (2015) combined the data of multiple ALMA Cycle 0 surveys from the archive to place upper limits on the [C II] luminosity function at $z \sim 4.5$. The upper limits are approximately three orders of magnitudes higher than the limits set by Swinbank et al., and do not constrain our predictions well.

### 5.5 Caveats

There are a few physical processes that were not included in this model which we discuss here.

#### 5.5.1 *X-ray-driven excitation*

Observations with the *Herschel Space Observatory* revealed strong excitation of high-J CO lines (CO J = 9–8 and higher) in nearby active galaxies (van der Werf et al. 2010; Meijerink et al. 2013). The high excitation lines can be explained by including the heating from X-ray radiation on top of the UV radiation. We did not include X-ray heating in our models. We limited the predictions for our CO luminosity function to CO J = 6–5, a regime where the contribution from X-ray heating to the CO luminosity is not thought to be dominant. The inclusion of X-ray heating could add to the luminosity of the higher rotational CO transitions such as CO J = 7–6 and up (see the CO SLEDs in Spaans & Meijerink 2008).

#### 5.5.2 *Mechanical heating and cosmic rays*

Mechanical heating through shocks increases excitation temperatures and decreases the optical depth at line centres (Kazandjian et al. 2015). Indeed, mechanical heating is needed to explain the excitation of CO in some local luminous infrared galaxies (e.g. Loenen et al. 2008; Meijerink et al. 2013; Rosenberg et al. 2014a,b).

A strong cosmic ray field can effectively destroy CO when the cosmic ray densities are 50–1000 times higher than in our own Milky Way, affecting the CO luminosity and CO-to-$H_2$ conversion rate of galaxies (Bayet et al. 2011; Meijerink et al. 2011; Bisbas, Papadopoulos & Viti 2015). This effect may already be important in Milky Way-like giant molecular clouds (Bisbas et al. 2015).

A proper inclusion of the effect of mechanical heating and cosmic rays (as well as X-ray-driven chemistry) would require a much more detailed chemistry model than currently is applied in this work.

#### 5.5.3 *[C II] emission from ionized regions*

[C II] emission can originate from different phases of the ISM. For instance, in our own Galaxy 80 per cent of the [C II] comes from atomic and molecular regions and 20 per cent from ionized gas (Pineda, Langer & Goldsmith 2014). For M17SW in the Milky Way, the fraction of [C II] from ionized regions is as high as 33 per cent (Pérez-Beaupuits et al. 2015).

These numbers can change from galaxy to galaxy and with redshift, depending on the properties of the ISM in a galaxy. In our work, we did not take the contribution from ionized regions to the [C II] emission of galaxies into account. Olsen et al. (2015b) applied a radiative transfer code to seven modelled main-sequence galaxies at $z = 2$. The authors compute the contribution to the total [C II] emission from PDRs, atomic, and ionized regions, and found that the [C II] emission from ionized regions only accounts for a few per cent of the total [C II] luminosity.

Observationally the fraction of [C II] emission in extragalactic sources arising from ionized regions is not well defined. Decarli et al. (2014a) showed for two Ly-$\alpha$ emitters at redshift $z = 4.7$ that the [C II]-to-[N II] ratio is consistent with the range of values expected for H II regions. This suggests that most of the [C II] emission comes from an ionized regime. On the other hand, Decarli et al. found that the [C II]-to-[N II] ratios in a sub-mm galaxy and quasi-stellar object at the same redshift are more consistent with a picture where a substantial fraction of the [C II] emission comes from a neutral regime. Gullberg et al. (2015) found for 20 dusty

star-forming galaxies that the CO and [C II] emission are consistent with PDR regions. Cormier et al. (2015) showed that [C II] emission from ionized regions becomes more important towards low-metallicity objects.

These observational results suggest that while we may be missing the contribution of H II regions in our [C II] predictions, these are likely not significant at least in the bright end of the luminosity function.

## 6 SUMMARY AND CONCLUSIONS

In this paper, we combined a semi-analytic model of galaxy formation with a radiative transfer code to make predictions for the evolution of the CO luminosity function, focusing on the CO J-transitions from J = 1–0 to J = 6–5 and [C II] out to $z = 6$.

(i) Our updated model successfully reproduces the observed scaling relations between CO luminosity and FIR luminosity/SFR out to CO J=6–5 at redshifts $z = 0, 1$, and 2, and between [C II] luminosity and FIR luminosity. Predicted luminosities for CO J = 7–6 up to CO J =9–8 are in reasonable agreement with observational constraints.

(ii) We reproduce the observational constraints for the CO luminosity function of galaxies at redshifts $z = 0$, $z = 0.3$, $z = 1.5$, and $z = 2.75$.

(iii) We provide predictions for CO luminosity functions out to $z = 6$. We find that the number densities of the CO luminosity functions increase from $z = 6$ to $z = 2$, and decrease at lower redshifts. This behaviour is closely linked to the history of the SFR density of our Universe. We predict that the CO-brightest galaxies can be observed at $z = 2$. CO J=2–1 and lower can be picked up by radio instruments, whereas CO J =3–2 and up are ideal to be observed by for instance ALMA and NOEMA.

(iv) We provide predictions for the [C II] luminosity function of galaxies out to $z = 6$. Similarly to CO, the [C II] luminosity function increases up to $z = 2$–3 and decreases at lower redshifts.

(v) Due to its brightness and moderate excitation density, the CO J=3–2 emission line is very favourable to observe the CO luminosity function and address the distribution of molecular gas in our Universe. This line can be picked up by ALMA at redshifts $z<3$ and by radio instruments at even higher redshifts. Nevertheless, care should be taken when converting the CO J = 3–2 luminosity function to a CO J = 1–0 luminosity function. The ratio between the characteristic luminosity describing the turning point between a power-law and exponential distribution for these two emission lines evolves with redshift.

(vi) The tension between the CO luminosity function at $z = 2.75$ and the [C II] luminosity function, and the observational constraints may be part of a bigger problem. Cosmological simulations have a hard time reproducing the gas content and CO emission of galaxies at intermediate redshifts. A suitable solution to solve some of the other problems that galaxy formation models face (mismatch between predicted and observed stellar mass functions and sSFR at intermediate redshift) should first be able to properly reproduce the gas content of galaxies out of which new stars are formed.

The results presented in this paper can serve as a theoretical framework for future deep field efforts with the next generation of radio and sub-mm instruments. They provide predictions for such surveys at the same time. Especially the survey speeds presented in Table 3 can be useful for the planning of future observational efforts. We look forward to future deep field that will be able to confront our predictions and place more constraints on the physics that drives galaxy formation.

## ACKNOWLEDGEMENTS

We thank the referee for a thorough report and very constructive comments that have improved the paper. GP thanks Matthieu Béthermin, Drew Brisbin, Caitlin Casey, Carl Ferkinhoff, Alex Karim, Desika Narayanan, and Fabian Walter for stimulating conversations. RSS thanks the Downsbrough family for their generous support, and acknowledges support from a Simons Investigator award.

## REFERENCES

Arrigoni M., Trager S. C., Somerville R. S., Gibson B. K., 2010, MNRAS, 402, 173
Barnes D. G. et al., 2001, MNRAS, 322, 486
Bayet E., Williams D. A., Hartquist T. W., Viti S., 2011, MNRAS, 414, 1583
Bigiel F., Blitz L., 2012, ApJ, 756, 183
Bigiel F., Leroy A., Walter F., Brinks E., de Blok W. J. G., Madore B., Thornley M. D., 2008, AJ, 136, 2846
Bisbas T. G., Papadopoulos P. P., Viti S., 2015, ApJ, 803, 37
Blitz L., Rosolowsky E., 2006, ApJ, 650, 933
Blumenthal G. R., Faber S. M., Flores R., Primack J. R., 1986, ApJ, 301, 27
Bolatto A. D., Wolfire M., Leroy A. K., 2013, ARA&A, 51, 207
Carilli C. L., Walter F., 2013, ARA&A, 51, 105
Carilli C. L. et al., 2015, preprint(arXiv:1510.06438)
Casey C. M. et al., 2015, preprint (arXiv:1510.06411)
Cormier D. et al., 2015, A&A, 578, A53
Crighton N. H. M. et al., 2015, MNRAS, 452, 217
de Looze I., Baes M., Bendo G. J., Cortese L., Fritz J., 2011, MNRAS, 416, 2712
da Cunha E. et al., 2013, ApJ, 766, 13
Daddi E. et al., 2010, ApJ, 713, 686
Daddi E. et al., 2015, A&A, 577, A46
Dannerbauer H., Daddi E., Riechers D. A., Walter F., Carilli C. L., Dickinson M., Elbaz D., Morrison G. E., 2009, ApJ, 698, L178
Davé R., Finlator K., Oppenheimer B. D., 2012, MNRAS, 421, 98
Decarli R. et al., 2014a, ApJ, 782, L17
Decarli R. et al., 2014b, ApJ, 782, 78
Eales S. et al., 2010, PASP, 122, 499
Federrath C., Klessen R. S., Schmidt W., 2008, ApJ, 688, L79
Feldmann R., Gnedin N. Y., Kravtsov A. V., 2012, ApJ, 747, 124
Flores R., Primack J. R., Blumenthal G. R., Faber S. M., 1993, ApJ, 412, 443
Genzel R. et al., 2010, MNRAS, 407, 2091
Giovanelli R. et al., 2005, AJ, 130, 2598
Gnedin N. Y., Kravtsov A. V., 2011, ApJ, 728, 88
Greve T. R. et al., 2014, ApJ, 794, 142
Grogin N. A. et al., 2011, ApJS, 197, 35
Gullberg B. et al., 2015, MNRAS, 449, 2883
Henriques B. M. B., White S. D. M., Thomas P. A., Angulo R., Guo Q., Lemson G., Springel V., Overzier R., 2015, MNRAS, 451, 2663
Herrera-Camus R. et al., 2015, ApJ, 800, 1
Hodge J. A., Riechers D., Decarli R., Walter F., Carilli C. L., Daddi E., Dannerbauer H., 2015, ApJ, 798, L18
Hollenbach D. J., Takahashi T., Tielens A. G. G. M., 1991, ApJ, 377, 192
Hopkins A. M., 2004, ApJ, 615, 209
Hopkins A. M., Beacom J. F., 2006, ApJ, 651, 142
Juneau S., Narayanan D. T., Moustakas J., Shirley Y. L., Bussmann R. S., Kennicutt R. C., Jr, Vanden Bout P. A., 2009, ApJ, 707, 1217
Kamenetzky J., Rangwala N., Glenn J., Maloney P. R., Conley A., 2015, preprint (arXiv:1508.05102)
Kazandjian M. V., Meijerink R., Pelupessy I., Israel F. P., Spaans M., 2015, A&A, 574, A127

Keres D., Yun M. S., Young J. S., 2003, ApJ, 582, 659
Koekemoer A. M. et al., 2011, ApJS, 197, 36
Komatsu E. et al., 2009, ApJS, 180, 330
Kravtsov A. V., 1999, PhD thesis, New Mexico State Univ.
Krumholz M. R., 2014, MNRAS, 437, 1662
Lagos C. d. P., Bayet E., Baugh C. M., Lacey C. G., Bell T. A., Fanidakis N., Geach J. E., 2012, MNRAS, 426, 2142
Lang P. et al., 2014, ApJ, 788, 11
Lemaster M. N., Stone J. M., 2008, ApJ, 682, L97
Leroy A. K., Walter F., Brinks E., Bigiel F., de Blok W. J. G., Madore B., Thornley M. D., 2008, AJ, 136, 2782
Leroy A. K. et al., 2009, AJ, 137, 4670
Lisenfeld U. et al., 2011, A&A, 534, A102
Liu D., Gao Y., Isaak K., Daddi E., Yang C., Lu N., van der Werf P., 2015, ApJ, 810, L14
Loenen A. F., Spaans M., Baan W. A., Meijerink R., 2008, A&A, 488, L5
Madau P., Dickinson M., 2014, ARA&A, 52, 415
Madau P., Ferguson H. C., Dickinson M. E., Giavalisco M., Steidel C. C., Fruchter A., 1996, MNRAS, 283, 1388
Matsuda Y., Nagao T., Iono D., Hatsukade B., Kohno K., Tamura Y., Yamaguchi Y., Shimizu I., 2015, MNRAS, 451, 1141
Meijerink R., Spaans M., 2005, A&A, 436, 397
Meijerink R., Spaans M., Loenen A. F., van der Werf P. P., 2011, A&A, 525, A119
Meijerink R. et al., 2013, ApJ, 762, L16
Mitra S., Davé R., Finlator K., 2015, MNRAS, 452, 1184
Mo H. J., Mao S., White S. D. M., 1998, MNRAS, 295, 319
Murray N., Rahman M., 2010, ApJ, 709, 424
Narayanan D., Krumholz M. R., 2014, MNRAS, 442, 1411
Narayanan D., Groppi C. E., Kulesa C. A., Walker C. K., 2005, ApJ, 630, 269
Narayanan D. et al., 2008, ApJS, 176, 331
Obreschkow D., Rawlings S., 2009, MNRAS, 394, 1857
Obreschkow D., Heywood I., Klöckner H.-R., Rawlings S., 2009, ApJ, 702, 1321
Oliver S. J. et al., 2012, MNRAS, 424, 1614
Olsen K. P., Greve T. R., Brinch C., Sommer-Larsen J., Rasmussen J., Toft S., Zirm A., 2015a, MNRAS, 457, 3306
Olsen K. P., Greve T. R., Narayanan D., Thompson R., Toft S., Brinch C., 2015b, ApJ, 814, 76
Ostriker E. C., Stone J. M., Gammie C. F., 2001, ApJ, 546, 980
Papadopoulos P. P., van der Werf P. P., Xilouris E. M., Isaak K. G., Gao Y., Mühle S., 2012, MNRAS, 426, 2601
Pérez-Beaupuits J. P., Wada K., Spaans M., 2011, ApJ, 730, 48
Pérez-Beaupuits J. P., Stutzki J., Ossenkopf V., Spaans M., Güsten R., Wiesemeyer H., 2015, A&A, 575, A9
Pilbratt G. L. et al., 2010, A&A, 518, L1
Pineda J. L., Langer W. D., Goldsmith P. F., 2014, A&A, 570, A121
Poelman D. R., Spaans M., 2005, A&A, 440, 559
Poelman D. R., Spaans M., 2006, A&A, 453, 615
Popping G., Caputi K. I., Somerville R. S., Trager S. C., 2012, MNRAS, 425, 2386
Popping G., Somerville R. S., Trager S. C., 2014a, MNRAS, 442, 2398 (PST14)
Popping G., Pérez-Beaupuits J. P., Spaans M., Trager S. C., Somerville R. S., 2014b, MNRAS, 444, 1301 (P14)
Popping G., Behroozi P. S., Peeples M. S., 2015a, MNRAS, 449, 477
Popping G. et al., 2015b, MNRAS, 454, 2258
Porter L. A., Somerville R. S., Primack J. R., Johansson P. H., 2014, MNRAS, 444, 942
Price D. J., Federrath C., Brunt C. M., 2011, ApJ, 727, L21
Prochaska J. X., Wolfe A. M., 2009, ApJ, 696, 1543
Robitaille T. P., Whitney B. A., 2010, ApJ, 710, L11
Rosenberg M. J. F., Kazandjian M. V., van der Werf P. P., Israel F. P., Meijerink R., Weiß A., Requena-Torres M. A., Güsten R., 2014a, A&A, 564, A126
Rosenberg M. J. F., Meijerink R., Israel F. P., van der Werf P. P., Xilouris E. M., Weiß A., 2014b, A&A, 568, A90
Rosenberg M. J. F. et al., 2015, ApJ, 801, 72
Schöier F. L., van der Tak F. F. S., van Dishoeck E. F., Black J. H., 2005, A&A, 432, 369
Sharon C. E., Baker A. J., Harris A. I., Thomson A. P., 2013, ApJ, 765, 6
Somerville R. S., Davé R., 2015, ARA&A, 53, 51
Somerville R. S., Primack J. R., 1999, MNRAS, 310, 1087
Somerville R. S., Primack J. R., Faber S. M., 2001, MNRAS, 320, 504
Somerville R. S., Hopkins P. F., Cox T. J., Robertson B. E., Hernquist L., 2008, MNRAS, 391, 481
Somerville R. S., Gilmore R. C., Primack J. R., Domínguez A., 2012, MNRAS, 423, 1992
Somerville R. S., Popping G., Trager S. C., 2015, MNRAS, 453, 4337 (SPT15)
Spaans M., Meijerink R., 2008, ApJ, 678, L5
Swinbank A. M. et al., 2012, MNRAS, 427, 1066
Tacconi L. J. et al., 2010, Nature, 463, 781
Tacconi L. J. et al., 2013, ApJ, 768, 74
Tunnard R., Greve T. R., 2016, ApJ, 819, 161
Vallini L., Gruppioni C., Pozzi F., Vignali C., Zamorani G., 2016, MNRAS, 456, L40
van der Werf P. P. et al., 2010, A&A, 518, L42
Walter F. et al., 2014, ApJ, 782, 79
Weiß A., Walter F., Scoville N. Z., 2005, A&A, 438, 533
White C. E., Somerville R. S., Ferguson H. C., 2015, ApJ, 799, 201
Wolfire M. G., Hollenbach D., McKee C. F., 2010, ApJ, 716, 1191

This paper has been typeset from a TEX/LATEX file prepared by the author.